

Testing AGN outflow and accretion models with C IV and He II emission line demographics in $z \approx 2$ quasars

Matthew J. Temple ^{1*}, James H. Matthews ^{2,3}, Paul C. Hewett ³, Amy L. Rankine ⁴,
Gordon T. Richards ⁵, Manda Banerji ⁶, Gary J. Ferland ⁷, Christian Knigge ⁶ and Matthew Stepney ⁶

¹Instituto de Estudios Astrofísicos, Universidad Diego Portales, Av. Ejército Libertador 441, Santiago 8370191, Chile

²Department of Physics, Astrophysics, University of Oxford, Denys Wilkinson Building, Keble Road, Oxford OX1 3RH, UK

³Institute of Astronomy, University of Cambridge, Madingley Road, Cambridge CB3 0HA, UK

⁴Institute for Astronomy, University of Edinburgh, Royal Observatory, Blackford Hill, Edinburgh EH9 3HJ, UK

⁵Department of Physics, Drexel University, 32 S. 32nd Street, Philadelphia, PA 19104, USA

⁶School of Physics & Astronomy, University of Southampton, Southampton SO17 1BJ, UK

⁷Department of Physics and Astronomy, The University of Kentucky, Lexington, KY 40506, USA

Submitted to MNRAS 2023 April 24

ABSTRACT

Using $\approx 190,000$ spectra from the seventeenth data release of the Sloan Digital Sky Survey, we investigate the ultraviolet emission line properties in $z \approx 2$ quasars. Specifically, we quantify how the shape of C IV $\lambda 1549$ and the equivalent width (EW) of He II $\lambda 1640$ depend on the black hole mass and Eddington ratio inferred from Mg II $\lambda 2800$. Above $L/L_{\text{Edd}} \gtrsim 0.2$, there is a strong mass dependence in both C IV blueshift and He II EW. Large C IV blueshifts are observed only in regions with both high mass and high accretion rate. Including X-ray measurements for a subsample of 5,000 objects, we interpret our observations in the context of AGN accretion and outflow mechanisms. The observed trends in He II and 2 keV strength are broadly consistent with theoretical Q_{SOSED} models of AGN spectral energy distributions (SEDs) for low spin black holes, where the ionizing SED depends on the accretion disc temperature and the strength of the soft excess. High spin models are not consistent with observations, suggesting SDSS quasars at $z \approx 2$ may in general have low spins. We find a dramatic switch in behaviour at $L/L_{\text{Edd}} \lesssim 0.1$: the ultraviolet emission properties show much weaker trends, and no longer agree with Q_{SOSED} predictions, hinting at changes in the structure of the broad line region. Overall the observed emission line trends are generally consistent with predictions for radiation line driving where quasar outflows are governed by the SED, which itself results from the accretion flow and hence depends on both the SMBH mass and accretion rate.

Key words: quasars: emission lines

1 INTRODUCTION

1.1 Observational context: spectroscopic properties of quasars

The spectroscopic properties of type-1 quasars have long been appreciated for their potential to provide insight into the physical processes responsible for luminous active galactic nuclei (AGN; Baldwin & Netzer 1978; Davidson & Netzer 1979; Kwan & Krolik 1981; Krolik & Kallman 1988; Elvis 2000). These processes include the excitation of various line- and continuum-emitting regions, and mechanisms for launching outflows which might ‘feed back’ energy to their host galaxies. Such processes are ultimately powered by accretion onto supermassive black holes (SMBHs; Lynden-Bell 1969), and thus depend primarily on the mass of the SMBH and the accretion rate, with potential second-order drivers including the spin of the SMBH and the metal content of the accreting material.

The search for insight has gained much from identifying and exploring the properties which are observed to vary the most. Such

diversity in the observed quantities must ultimately be driven by some of the physics which we would like to use to better constrain both the growth of SMBHs and their effect on the galactic ecosystems in which they reside. The most famous result of these investigations is arguably the identification of the so-called ‘eigenvector 1’ (EV1), which accounts for the largest amount of correlated variance in the optical spectra of low-redshift ($z < 1$) type-1 AGN spectra. Most authors now agree that the EV1 is driven by the mass-normalised accretion rate (the Eddington ratio), possibly convolved with some orientation effect (Boroson & Green 1992; Wills et al. 1999; Sulentic et al. 2000; Shen & Ho 2014; Sun & Shen 2015; Sulentic & Marziani 2015; Wolf et al. 2020).

Similarly, the ultraviolet emission features in quasar spectra also show a rich phenomenology (Croom et al. 2002; Jensen et al. 2016; Brodzeller & Dawson 2022). Early work by Baldwin (1977) showed that the equivalent widths (EWs) of various ultraviolet lines, most notably C IV $\lambda 1549$, were anti-correlated with the ultraviolet continuum luminosity. Shang et al. (2003) showed that this ‘Baldwin effect’ was independent of EV1 in 22 quasars with $z < 0.4$, implying different physical drivers for these correlations. Early observations also

* E-mail: Matthew.Temple@mail.udp.cl

demonstrated that the centroid of the C iv emission line is commonly shifted to the blue (Gaskell 1982; Wilkes 1984; Richards et al. 2002). Within a sample of 87 Palomar-Green quasars, Baskin & Laor (2004, 2005) found that large C iv blueshifts were only seen in objects with high Eddington ratios, although not all quasars with high Eddington ratios had large C iv blueshifts. The EV1 formalism was extended by Bachev et al. (2004) and Sulentic et al. (2007) to include the velocity shift of C iv, again finding that large C iv blueshifts are seen only in so-called ‘Population A’ quasars with high Eddington ratios.

With the start of the Sloan Digital Sky Survey (SDSS; York et al. 2000), large samples of rest-frame ultraviolet quasar spectra became available. Equally as important were methods to accurately characterize the systemic redshift of each quasar (Hewett & Wild 2010), which is necessary to infer the velocity shift of any emission features. A notable work by Richards et al. (2011) summarized the state of the field a decade ago at the time of the seventh data release (DR7; Schneider et al. 2010) from SDSS. Using $\approx 35\,000$ quasar spectra, Richards et al. (2011) confirmed the Baldwin effect and showed that the EW of C iv line also anti-correlates with the magnitude of the C iv blueshift: quasars with higher luminosities show, on average, weaker C iv emission which is more strongly blueshifted. C iv blueshifts could be a signature of emission from ionized gas being driven away from the accretion disc along the line-of-sight to the observer (Leighly & Moore 2004), in which case the results of Richards et al. (2011) can be interpreted as brighter objects showing stronger emission from outflowing gas and weaker emission from the virialized broad line region (BLR). We discuss this interpretation further in Section 5.2.2, but do not assume anything about the origin of C iv line shifts when presenting our observational results in Section 4.1.

Richards et al. (2011) also demonstrated that the C iv properties are strongly correlated with the EW of the nearby He II $\lambda 1640$ emission line. More recent work by Rankine et al. (2020) has shown that the correlations between the EW of He II and both the EW and blueshift of C iv are also present in quasars with broad absorption features. We now know that the C iv and He II properties are strongly correlated with the properties of other ultraviolet emission features such as Ly α , N v, Si iv and O iv] (Temple et al. 2021b), Fe III, Al III, Si III] and C III] (Temple et al. 2020), as well as the optical [O III] emission (Vietri et al. 2018; Coatman et al. 2019; Vietri et al. 2020), the strength of near infrared emission from dust at the sublimation temperature (Temple et al. 2021a), the strength of the far infrared emission (Maddox et al. 2017), the radio detection fraction (Rankine et al. 2021) and the strength of the 2 keV X-ray continuum (Kruczek et al. 2011; Zappacosta et al. 2020; Timlin et al. 2020, 2021; Lusso et al. 2021; Marlar et al. 2022; Rivera et al. 2022). Tentative links have also been found between the C iv blueshift and the amount of continuum reddening ascribed to nuclear dust (Calistro Rivera et al. 2021; Fawcett et al. 2022).

The existence of such correlations - between parameters which trace emission at different wavelengths and from different physical regions - suggests that they are driven (either directly or indirectly) by changes in some of the fundamental physical parameters which govern the properties of a SMBH and its surrounding regions, such as the SMBH mass, spin, and accretion rate. The space spanned by C iv blueshift and C iv EW therefore appears to be just as important as EV1 in understanding the physics of luminous AGN. However, while the location of a given quasar spectrum on either EV1 or the C iv blueshift–EW space must ultimately be a function of the fundamental SMBH parameters, there is no guarantee that such a function is linear, or even injective (i.e. one-to-one with a well-defined inverse). For example, we cannot rule out the possibility that two objects with

different M_{BH} and accretion rate have similar (or indeed identical) C iv emission.

1.2 Theoretical context: AGN outflows and SEDs

Mass outflows from AGN can be launched by thermal pressure, magnetic forces, or radiation (Laha et al. 2021). Thermal winds can only be launched at large radii [$R \gtrsim 10^5 R_g \approx 5 \times (M_{\text{BH}}/10^9 M_\odot)$ parsec] with terminal velocities of order $100\text{--}1000 \text{ km s}^{-1}$ (Begelman et al. 1983; Woods et al. 1996; Mizumoto et al. 2019). Faster outflows with speeds $> 2000 \text{ km s}^{-1}$, as commonly seen in broad high-ionization ultraviolet absorption features, are most likely launched on smaller (sub-parsec) scales. Magnetically driven winds (Blandford & Payne 1982; Emmering et al. 1992; Konigl & Kartje 1994; Fukumura et al. 2010; Yang et al. 2021a) may be important in this context, but we currently lack predictive models for how such winds would translate into observable quantities (although see e.g. Bottorff et al. 2000; Chajet & Hall 2013). On the other hand, radiation line driving (Castor et al. 1975; Murray et al. 1995; Murray & Chiang 1995; Elvis 2000; Proga et al. 2000; Proga & Kallman 2004; Proga 2007; Risaliti & Elvis 2010; Elvis 2017; Nomura & Ohsuga 2017; Nomura et al. 2020; Zhu et al. 2022) is intrinsically linked to the spectral energy distribution (SED) of the continuum which is responsible for both ionizing the transitions and then accelerating the flow by providing the source of radiation pressure. By considering how the SED changes with SMBH mass and accretion rate, authors such as Giustini & Proga (2019) have developed unifying frameworks which make testable predictions for luminous AGN based on the physics of radiation line driven winds.

The ionizing continuum SED depends on the structure of the accretion flow, which in turn is set by the SMBH mass M_{BH} , the mass-normalised accretion rate $\dot{m} = \dot{M}_{\text{BH}}/\dot{M}_{\text{Edd}}$ and the SMBH spin a_* . Empirically, the optical–to–X-ray SEDs of AGN are seen to contain at least three distinct components (Elvis et al. 1994; Casebeer et al. 2006; Leighly et al. 2007; Done et al. 2012; Jin et al. 2012). First, any optically thick accretion disc will emit thermally, with larger radii being cooler, giving rise to a multi-temperature blackbody which is expected to peak in the near-ultraviolet ($M_{\text{BH}} > 10^8 M_\odot$), far-ultraviolet or soft X-rays ($M_{\text{BH}} < 10^8 M_\odot$). This peak would be expected to depend on M_{BH} if larger SMBHs have accretion flows which truncate at lower temperatures (eq. 5.3.1 of Novikov & Thorne 1973). However, this part of the SED is instead commonly observed to peak around 1100 \AA (Shang et al. 2005; Krawczyk et al. 2013; Stevans et al. 2014; Vanden Berk et al. 2020), albeit with lower luminosity AGN showing harder continuum emission at $\lambda < 1100 \text{ \AA}$ (Telfer et al. 2002; Scott et al. 2004). The uniformity of this peak wavelength across a wide range of M_{BH} and \dot{m} has been suggested to result from opacity effects (Czerny & Elvis 1987) or from line-driven winds which remove mass from the inner accretion disc (Slone & Netzer 2012; Laor & Davis 2014). Second, a hot Comptonised ‘corona’ emits a non-thermal power law which dominates the X-ray continuum above 1 keV (Haardt & Maraschi 1991; Titarchuk 1994). Finally, a ‘soft excess’ is seen in the X-rays below $\approx 1 \text{ keV}$, which is usually attributed to an intermediate warm Comptonising component (Petrucci et al. 2018, 2020). This soft excess may be a significant contributor to the ionizing SED in the $\approx 100\text{--}1000 \text{ \AA}$ ($\approx 10\text{--}100 \text{ eV}$) range, where many of the ultraviolet transitions are excited, but where direct observations of the continuum are not possible due to the high opacity of neutral hydrogen along the line-of-sight.

For a line-driven disc-wind to emerge, the system needs strong ultraviolet emission to produce sufficient radiation pressure, but also

a soft enough SED to avoid over-ionizing the gas (Murray et al. 1995; Higginbottom et al. 2014). For each relevant line, the flux at the line energy combined with the line opacity determines the line-driving boost beyond radiation pressure from Thomson scattering. The line opacity depends on the ionization state, which is primarily sensitive to the flux at the ionization edges (48 and 64 eV for the production and destruction of C IV). Line driving results when this effect is summed across many lines, each with their own energies, leading to a complex interplay between the flux of the SED underneath all the relevant lines in the ultraviolet and the flux of the SED beyond all the relevant ionization edges. Giustini & Proga (2019) suggest that both $L/L_{\text{Edd}} \gtrsim 0.25$ and $M_{\text{BH}} \gtrsim 10^8 M_{\odot}$ are required to satisfy these criteria and hence to power a strong outflow through radiation line driving. Giustini & Proga (2019) also expect the M_{BH} dependence of the observed outflow properties to be different above and below an \dot{m} of around 0.25, where they expect the cold, optically thick accretion disc to extend down towards the innermost stable circular orbit (ISCO) and replace the hot, optically thin, inner accretion flow which is present at lower accretion rates. In other words, they require $L/L_{\text{Edd}} \gtrsim 0.25$ to ensure emission from thermal disc emission dominates over that from the hot corona, to accelerate a strong line-driven wind without over-ionizing the gas. With the quantity and quality of spectroscopic data which are now available from large surveys, these predictions from the Giustini & Proga (2019) framework can be tested empirically.

1.3 Observational probes of quasar SEDs

From an observational viewpoint, it is relatively easy to constrain the SED of an unobscured type-1 AGN in the rest-frame infrared, optical and X-ray wavebands, as photometric measurements can place direct constraints on the emission. For example, the strength of the rest-frame 2 keV X-ray continuum relative to the near-ultraviolet continuum has been shown to anti-correlate with the ultraviolet continuum luminosity in the so-called $\alpha_{\text{ox}}-L_{2500\text{\AA}}$ relation (Avni & Tananbaum 1982, 1986; Steffen et al. 2006; Just et al. 2007; Lusso & Risaliti 2016; Timlin et al. 2021), and the fractional contribution of the 2-10 keV emission to the total bolometric power of the AGN is known to vary as a function of the accretion rate \dot{m} (Vasudevan & Fabian 2007, 2009). However, while this X-ray waveband can make an important contribution to the total emitted energy, it contributes a negligible number of ionizing photons to the photoionization budget of the BLR gas (see Appendix A). The number of ionizing photons is instead dominated by photons at the ionization edges themselves, which is of the order of 10-100 eV for the ultraviolet BLR (e.g. production and destruction edges of 7.6 and 15 eV for Mg II, 48 and 64 eV for C IV, and 24 and 54 eV for He II; see also fig. 13 of Richards et al. 2011). This extreme ultraviolet (EUV) part of the SED is not directly observable due to intervening absorption along the line-of-sight, but plays a crucial role in the physics of the BLR. To add to the complexity, the relative contribution of the warm Comptonising soft excess to the total EUV emission is likely to be varying as a function of M_{BH} and \dot{m} , meaning that the observable 2 keV continuum may not be a reliable proxy for the strength of the EUV SED at the ionization edges.

C IV is a resonant doublet transition with a complicated ionic structure, so the strength of C IV emission is not necessarily a good tracer of the ionizing SED. However, it is instead possible to probe the EUV continuum using the He II $\lambda 1640$ recombination line, which arises from a simple hydrogenic (i.e. single electron) system. Under the assumptions that the He II emitting region is in equilibrium and that the He II continuum is optically thick, the total rate of He II-

ionizing photons must balance the total number of recombinations such that each He II $\lambda 1640$ line photon can be associated with an ionizing continuum photon at or above 54 eV. This method was first used by Zanstra (1929) to infer stellar temperatures using the strength of Hydrogen recombination lines (section 5.10 of Osterbrock & Ferland 2006). Following previous works (Mathews & Ferland 1987; Baskin et al. 2013; Ferland et al. 2020; Timlin et al. 2021), we will use the strength of He II as a proxy for the strength of the ‘unseen’ EUV continuum which is ionizing the BLR.

1.4 This work

The first goal of this paper is to provide an up-to-date summary of our knowledge of the ultraviolet spectral properties of type-1 quasars, using the final data release (DR17) from the fourth iteration of SDSS. This sample contains an order of magnitude more quasars than the SDSS DR7 sample used by Richards et al. (2011). The large sample size allows us to consider the emission properties as a function of both mass and Eddington ratio simultaneously, and thus provide a test of model quasar SEDs from Kubota & Done (2018) and of current theories of radiation line-driven AGN winds (Giustini & Proga 2019), which is our second goal.

To best compare with theory and simulations, we present observed quantities such as the C IV blueshift, He II EW, and α_{ox} as a function of three physical parameters: the ultraviolet continuum luminosity, the SMBH mass estimated from the Mg II $\lambda 2800$ emission line, and the inferred Eddington ratio. This relatively simple exercise has long been used to gain insight into the physics of AGN (Dibai 1980), but is subtly different from purely empirical approaches which observe trends in emission line properties (e.g. EV1 or the C IV blueshift-EW plane) and then try to infer which underlying physical parameters are driving those trends. By contrast, theoretical models make predictions for the SED and outflow properties as a function of the SMBH mass and accretion rate. In this work we confront such predictions directly with observations, showing that the ultraviolet emission lines display different behaviour above a threshold of $L_{\text{bol}}/L_{\text{Edd}} \approx 0.2$, consistent with predictions for radiation line-driven winds, and finding good qualitative agreement between the Kubota & Done (2018) SED models and observed continuum tracers in regions of parameter space where their models were not calibrated.

The structure of this paper is as follows. In Section 2 we present the observational data, while in Section 3 we describe the SED models to which we compare. We present our key results in Section 4 and discuss their implications and limitations in Section 5. Throughout this work, wavelengths are given in vacuum in units of Ångströms, and we assume a flat Λ CDM cosmology with $\Omega_m = 0.27$, $\Omega_{\Lambda} = 0.73$ and $H_0 = 71 \text{ km s}^{-1} \text{ Mpc}^{-1}$. Energies, frequencies and wavelengths are given in the rest-frame unless stated otherwise.

2 OBSERVATIONAL DATA

2.1 Rest-frame ultraviolet spectra

The first aim of this paper is to quantify the behaviour of He II $\lambda 1640$ and C IV $\lambda 1549$ as a function of SMBH mass M_{BH} and Eddington ratio L/L_{Edd} . The M_{BH} inferred from single-epoch measurements of C IV is known to be biased as a function of the emission line properties (Baskin & Laor 2005; Shen et al. 2008; Coatman et al. 2016, 2017; Mejía-Restrepo et al. 2018), so we will instead use the velocity width of the Mg II $\lambda 2800$ line to infer M_{BH} . We construct

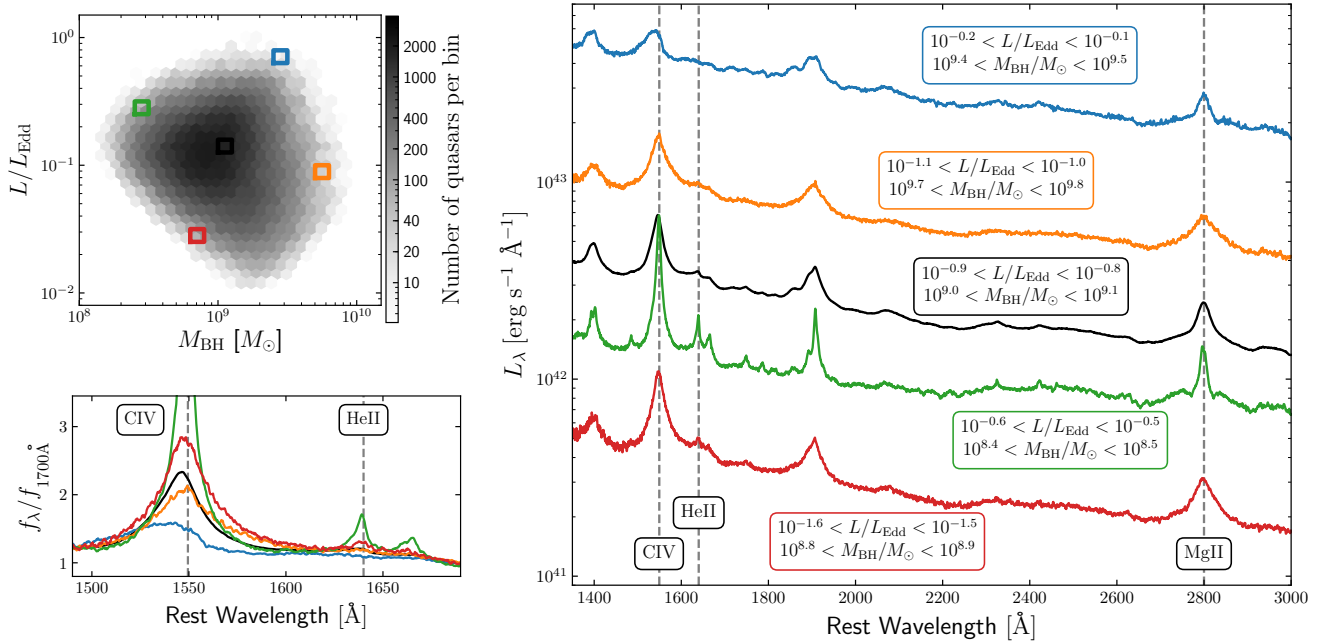


Figure 1. *Top left panel:* the distribution of our sample of 186 303 quasars with redshifts $1.5 < z < 2.65$ in the $M_{\text{BH}}-L/L_{\text{Edd}}$ plane. Throughout this work, we only consider hexagonal bins where there are five or more quasars per bin. By construction, the FWHM of $\text{Mg II } \lambda 2800$ increases from top-left to bottom-right of this parameter space, while the 3000 Å continuum luminosity increases from bottom-left to top-right. *Right panel:* composite spectra taken from the different regions of the $M_{\text{BH}}-L/L_{\text{Edd}}$ plane indicated in the top left panel. In black is shown a composite from the densely populated region in the centre of the $M_{\text{BH}}-L/L_{\text{Edd}}$ plane. The coloured composites were chosen to illustrate the full diversity of emission line properties which can be seen with changing SMBH mass and Eddington ratio. *Bottom left panel:* comparing the composite spectra in the region around $\text{C IV } \lambda 1549$ and $\text{He II } \lambda 1640$. Here the spectra have been normalised at 1700 Å and plotted on a linear y-axis. The EW of He II can be seen to correlate with the profile of C IV : the high-mass, high-Eddington composite in blue displays weak lines and blueshifted C IV while the low-mass, high-Eddington composite in green shows much stronger line emission with no blue excess in C IV , consistent with fig. 11 of Richards et al. (2011) and fig. A2 of Rankine et al. (2020). The difference here is that, instead of being constructed from C IV or C III emission properties, objects were included based on the FWHM of Mg II and L_{3000} to represent regions of the $M_{\text{BH}}-L/L_{\text{Edd}}$ plane, and also that the larger sample from SDSS DR17 includes fainter objects such as those contributing to the composite in red. Composite spectra spanning the full range of the $M_{\text{BH}}-L/L_{\text{Edd}}$ space are available as supplemental online-only material with the journal.

a sample of quasars from the SDSS with coverage of rest-frame wavelengths 1450–3000 Å to include C IV , He II and Mg II (Fig. 1).

The original selection of the SDSS DR17 quasar sample was described by Lyke et al. (2020) and Abdurro’uf et al. (2022). We post-process each spectrum using a sky subtraction routine conceptually similar to that described by Wild & Hewett (2005)¹. Systemic redshifts are calculated as described in section 3 of Rankine et al. (2020). Our redshift estimation routine uses the rest-frame 1600–3000 Å region, deliberately excluding the C IV emission line, which is a key difference compared to the approach employed in the SDSS quasar catalogues. The improved redshifts and sky-subtracted spectra will be described in a forthcoming publication by P. C. Hewett. To measure the emission line properties, we employ the spectral reconstructions from the Mean-Field Independent Component Analysis (ICA) carried out by Rankine et al. (2020), which we have successfully used in our previous investigations into quasar emission line physics (Temple et al. 2020, 2021a,b). Ten spectral ICA components are used to reconstruct each spectrum, using an iterative routine to mask absorption features while fitting linear combinations of the components to the data. The ICA-reconstructions provide a significant improvement

in the measurement of emission line properties, reducing the impact of the modest signal-to-noise ratio (S/N) in the original spectra and the effect of weak absorption lines (e.g. intervening or outflowing $\text{C IV } \lambda \lambda 1548, 1550$ doublets). We exclude objects with broad low-ionization absorption features, as such absorption features may affect the Mg II emission line (in the case of LoBALs), or lead to a sub-optimal reconstruction of the C IV line (in the case of FeLoBALs). A small fraction (< 1 per cent) of the sample was excluded either because the ICA failed to converge, or because the resulting reconstruction had reduced $\chi^2 > 2$, as described in section 4.3 of Rankine et al. (2020). To include both C IV and Mg II in the observed spectrum, we limit our sample to redshifts $1.5 < z < 2.65$. Spectra from before the start of the BOSS survey (MJD 55000) were observed using the original SDSS spectrograph which had a more limited wavelength coverage; for these objects we require $1.6 < z < 2.2$ to ensure coverage of C IV and Mg II . Each quasar spectrum is required to possess a mean S/N (per 69 km s^{-1} SDSS pixel) ≥ 3.0 over the rest-frame interval 1700–2200 Å. These criteria leave a sample of 186 303 quasars.

C IV and He II emission properties are measured consistently with Richards et al. (2011) and Rankine et al. (2020). To compute the EW of C IV emission, a power law continuum is defined using the median flux in the 1445–1465 and 1700–1705 Å wavelength windows. This continuum is then subtracted from the spectrum to isolate the line flux in the 1500–1600 Å wavelength region. The He II EW is measured

¹ Measurements of spectrum properties derived from observed-frame wavelengths > 6700 Å improve somewhat but none of the results, or conclusions, of this paper change if the original DR17 reductions of the spectra are used instead.

in the same way across the 1620-1650 Å wavelength region, using windows at 1610-1620 and 1700-1705 Å to define the continuum model. The C IV emission line ‘blueshift’ is defined as the Doppler shift of the wavelength bisecting the continuum-subtracted line flux:

$$\text{C IV blueshift} \equiv c \times \left(\frac{\lambda_{\text{rest}} - \lambda_{\text{median}}}{\lambda_{\text{rest}}} \right) \quad (1)$$

where c is the speed of light, λ_{median} is the rest-frame wavelength of the observed line centroid, and $\lambda_{\text{rest}} = 1549.48 \text{ \AA}$ is the mean rest-frame wavelength of the C IV $\lambda\lambda 1548.19, 1550.77$ doublet.

2.2 X-ray data

In addition to the rest-frame ultraviolet emission features, we can use the rest-frame 2 keV X-ray continuum emission to gain further insight into the SEDs of the quasars in our sample. We therefore cross-match our sample of 186 303 objects to various X-ray catalogues from the literature, in order to build a large sample of rest-frame 2 keV measurements. 4000 objects from our sample of $1.5 < z < 2.65$ objects with ultraviolet spectra are included in the recent study of quasar X-ray properties by Rivera et al. (2022), including 2691 with *XMM-Newton* observations from Lusso et al. (2020), 1291 with *Chandra* observations from Timlin et al. (2020), and 18 with *XMM-Newton* observations from Liu et al. (2020). 972 sources in our sample have X-ray data from the *eROSITA* Final Equatorial Depth Survey (eFEDS; Liu et al. 2022): 757 objects from the SDSS DR16 quasar catalogue (Lyke et al. 2020) and 215 sources with spectra released in SDSS DR17 (Abdurro’uf et al. 2022). We use data from the second ROSAT All-Sky Survey (2RXS; Boller et al. 2016) for objects included in the SDSS DR16 SPIDERS programme (Dwelly et al. 2017; Comparat et al. 2020). The flux limit for this survey is relatively bright so we use the Bayesian measurements described by Coffey et al. (2019) which account for the Eddington bias. A total of 36 objects from 2RXS are included in our sample. Finally, we include 7, 9, and 7 objects with *Chandra* observations from Timlin et al. (2021), Ni et al. (2018, 2022) and Fu et al. (2022) respectively. These last three sub-samples were selected to have high L_{UV} , weak C IV and strong C IV respectively, but the number of quasars is small and our results would be unchanged if we were to exclude them.

The compilation results in a sample of 5031 quasars with measurements of both their ultraviolet (2500 Å) and X-ray (2 keV) continuum fluxes. We use the rest-frame 2 keV fluxes reported by Ni et al. (2018, 2022), Coffey et al. (2019), Timlin et al. (2021), Fu et al. (2022), Liu et al. (2022), and Rivera et al. (2022), without any restriction on the spectral slope. However, we have verified that the conclusions of this work would not change if we excluded objects which may be affected by absorption. From these fluxes we compute luminosities assuming a consistent cosmology (Section 1.4) across all sub-samples. We then infer α_{ox} , the logarithm of the ratio of the rest-frame 2 keV and 2500 Å monochromatic luminosities:

$$\alpha_{\text{ox}} = \log_{10}(\nu L_{\nu})_{2\text{keV}} - \log_{10}(\nu L_{\nu})_{2500\text{\AA}}, \quad (2)$$

as a measure of the relative strength of the X-ray emission in each source. Objects with smaller (i.e. more negative) α_{ox} have weaker 2 keV X-ray emission relative to the ultraviolet continuum.

2.3 Black hole masses and Eddington ratios

We estimate SMBH masses using the single-epoch virial estimator described by Vestergaard & Osmer (2009), using the full width at

half maximum (FWHM) of the Mg II line:

$$M_{\text{BH}} = 10^{6.86} \left(\frac{\text{FWHM}(\text{Mg II})}{1000 \text{ km s}^{-1}} \right)^2 \left(\frac{L_{3000}}{10^{44} \text{ erg s}^{-1}} \right)^{0.5} M_{\odot}. \quad (3)$$

where L_{3000} is the rest-frame monochromatic continuum luminosity νL_{ν} at 3000 Å. This M_{BH} estimator assumes a relationship between the radius of the Mg II-emitting region and the observed L_{3000} which is independent of the shape of the ionizing SED, or more generally, independent of any changes in the accretion disc structure which may arise with changing M_{BH} or accretion rate. We discuss this assumption further in Section 5.1.2. We infer the FWHM of Mg II from our ICA reconstructions, which provide a more robust model of the intrinsic Mg II profile than a conventional Gaussian fit in low S/N spectra. Using a sub-sample with $S/N > 10$, we have verified that our Mg II FWHM measurements are consistent with those obtained from fitting a single Gaussian to Mg II together with an iron template (Vestergaard & Wilkes 2001) using the routine described by Shen et al. (2011). The key results of this paper would not change if we were to instead use such a Gaussian model for Mg II, but there would be significantly more scatter in lower luminosity regions of parameter space where the spectral S/N is poorer on average. The error budget on our resulting M_{BH} is dominated by the 0.55 dex uncertainty on the single-epoch estimator as described by Vestergaard & Osmer (2009).

We infer L_{3000} by fitting a quasar SED model (Temple et al. 2021c) to *griz* photometry. For sources in SDSS DR16 we use the SDSS photometry reported by Lyke et al. (2020), and for eFEDS-selected sources in SDSS DR17 we use the Hyper-Suprime Cam photometry reported by Salvato et al. (2022). Eddington luminosities are calculated in the usual way, balancing the gravitational and radiation forces in a Hydrogen-only plasma, and assuming the dominant source of opacity is Thomson electron scattering:

$$L_{\text{Edd}} = \frac{4\pi G M_{\text{BH}} m_{\text{p}} c}{\sigma_{\text{T}}} = 1.26 \times 10^{38} \left(\frac{M_{\text{BH}}}{M_{\odot}} \right) \text{ erg s}^{-1}. \quad (4)$$

The Eddington ratio $L_{\text{bol}}/L_{\text{Edd}}$ (hereafter L/L_{Edd}) is then estimated assuming a constant bolometric correction of $L_{\text{bol}} = 5.15 \times L_{3000}$. We discuss this assumption further in Section 5.1.1, and show how our key observables depend directly on FWHM(Mg II) and L_{3000} in Appendix B.

Our sample of 186 303 quasars spans 2.5 dex in luminosity, with $L_{3000} \approx 10^{44.5-47} \text{ erg s}^{-1}$ and $L_{\text{bol}} \approx 10^{45-47.5} \text{ erg s}^{-1}$. We infer SMBH masses in the $10^8-10^{10} M_{\odot}$ range and Eddington ratios from 0.01 to unity, with the distribution of our sample shown in Fig. 1.

3 MODELING THE QUASAR SED

Our second goal is to confront observational data with models for accretion and outflow in quasars; more specifically, we aim to test if the changes in observed emission line and continuum properties with M_{BH} and Eddington ratio are consistent with QSOSED² models (Kubota & Done 2018) for the SED of the ionizing continuum. We used the implementation of QSOSED in XSPEC (Arnaud 1996) to calculate SEDs, via the PYXSPEC python wrapper (Gordon & Arnaud 2021).

In QSOSED, the radiation originates from three characteristic regions: an outer thermal disc, an inner hot Comptonising ‘corona’ and an intermediate warm Comptonising component. These three

² <https://heasarc.gsfc.nasa.gov/xanadu/xspec/manual/node132.html>

regions are assumed to be radially stratified as defined by four critical radii: $R_{\text{ISCO}} < R_{\text{hot}} < R_{\text{warm}} < R_{\text{out}}$. The inner and outer radii are defined by the radius of the innermost stable circular orbit R_{ISCO} and the self-gravitation radius R_{out} . The hot X-ray component originates from $R_{\text{ISCO}} < R < R_{\text{hot}}$, and has a luminosity set by the sum of the directly dissipated power, $L_{\text{diss,hot}}$, and the seed photon luminosity, L_{seed} . One of the key aspects of the model is the empirically motivated assumption that the dissipated power is always 2 per cent of the Eddington luminosity; this constraint defines the value of R_{hot} . The outer radius of the warm Comptonising component R_{warm} is set to be twice R_{hot} . For $R_{\text{warm}} < R < R_{\text{out}}$, the thermal disc component is assumed to emit as described by Novikov & Thorne (1973).

QSOSED has four physical input parameters: the cosine of the inclination, $\cos i$, the SMBH mass, M_{BH} , the dimensionless spin parameter, a_* , and the Eddington-scaled accretion rate, $\dot{m} \equiv \dot{M}_{\text{acc}}/\dot{M}_{\text{Edd}}$. We fix $\cos i = 0.5$ and calculate grids of models in (M_{BH}, \dot{m}) parameter space, for non- and maximally-spinning SMBHs $a_* \in (0, 0.998)$. We calculate models with 21 logarithmically-spaced grid points in each direction, spanning the ranges $8 \leq \log(M_{\text{BH}}/M_{\odot}) \leq 10$ and $-1.65 \leq \log \dot{m} \leq 0$, corresponding to intervals of 0.1 and 0.0825 dex. To compare with observations, we take the input SMBH mass and calculate the Eddington ratio from L_{3000} using the same bolometric correction of 5.15 that we apply to the observational data (but see Section 5.1.1 and Appendix C). Here, and in Section 4.2, we present models for only the non-spinning case, as these are in much better agreement with the data. We discuss the impact of SMBH spin and system inclination in Section 5.2.3 and models with $a_* = 0.998$ are presented in Appendix D.

Although the emission line properties must depend on the ionizing SED, the exact relationship between, for example, C IV EW and the SED is complex due to a number of confounding factors such as BLR geometry, density and radiative transfer. The relationship to any kinematic signatures such as C IV blueshift is even more complicated and would require a physical model for the line formation region and associated flow dynamics. A somewhat simpler case is the EW of He II $\lambda 1640$, which is a recombination line and therefore a reasonable ‘photon counter’. He II has history as a tracer of the EUV continuum: for example, in cataclysmic variables Hoare & Drew (1991) applied a modified Zanstra (1929) method to infer boundary layer temperatures, and in quasars, Leighly (2004) note that a high He II EW is indicative of a strong X-ray continuum. Assuming Case B recombination, Mathews & Ferland (1987) give the He II $\lambda 1640$ EW in terms of the 228 Å continuum flux. Their equation can be inverted to give the proportionality

$$\frac{F_{\nu}(\lambda 228)}{F_{\nu}(\lambda 1640)} \propto \text{EW}(\text{He II } \lambda 1640) \frac{\Omega}{4\pi}, \quad (5)$$

where $\Omega/4\pi$ is the covering fraction and the proportionality constant is dependent on the shape of the SED (Mathews & Ferland 1987 considered a power law in F_{ν} at 228 Å). In this work we assume, based on the above equation, that the observed He II $\lambda 1640$ EW is a reasonable proxy for the ratio of continuum luminosities L_{228}/L_{1640} .

In Fig. 2 we present output SEDs from QSOSED, in which the three radially stratified components can be seen as separate ‘bumps’ in the spectrum. In these plots, we show how the model SEDs change as a function of Eddington-scaled accretion rate, \dot{m} (for fixed mass, top panel) and SMBH mass, M_{BH} (for fixed \dot{m} , bottom panel). The important frequencies for determining He II EW (corresponding to 228 Å and 1640 Å) and α_{ox} (corresponding to 2500 Å and 2 keV) are marked. Increasing \dot{m} increases the overall luminosity of the system and pushes the peak of the outer thermal disc component to higher frequencies. Simultaneously, the hard X-ray slope becomes

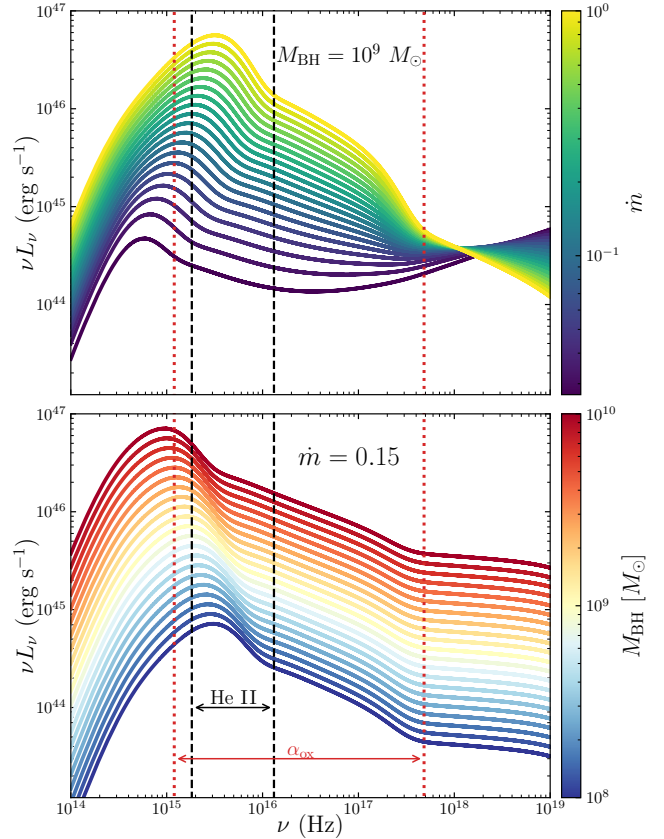


Figure 2. Output SEDs in νL_{ν} units from QSOSED for $a_* = 0$ and $\cos i = 0.5$. The vertical lines show, from left to right, the frequencies at 2500 Å, 1640 Å, 228 Å ($= 54$ eV) and 2 keV which together determine α_{ox} and the EW of He II $\lambda 1640$. The He II ionization edge at 54 eV (1.3×10^{16} Hz) lies in the EUV regime where the intermediate warm Comptonising component in QSOSED is most important, but the EW of He II can also be seen to depend on the location of the peak of the ionizing SED. *Top panel:* SEDs with fixed SMBH mass of $10^9 M_{\odot}$ and varying \dot{m} in logarithmic intervals. As \dot{m} increases the peak of the SED moves to the blue, the luminosity increases, and the hard X-ray power law spectral index becomes softer. *Bottom panel:* SEDs with fixed $\dot{m} = 0.15$ and varying M_{BH} in logarithmic intervals. As SMBH mass increases the peak of the SED moves to the red, and the luminosity increases. A maximal spin analogue to this plot is shown in Fig. D1.

significantly softer and $L_{2\text{keV}}$ only increases slowly, consistent with eq. 6 and fig. 5b of Kubota & Done (2018). As a result, the higher Eddington fraction objects are more X-ray weak relative to their ultraviolet flux. Increasing M_{BH} also increases the total luminosity, but now the peak of the thermal component moves to lower frequencies and the hard X-ray slope stays fairly constant. In both panels of the plot the peak of the SED can be found on either side of the low frequency pivot points for both He II EW and α_{ox} , resulting in an interesting interplay between these quantities and the fundamental AGN parameters.

4 RESULTS

4.1 Observed properties in $M_{\text{BH}}-L/L_{\text{Edd}}$ space

The first observational result from this work is the behaviour of the C IV $\lambda 1549$ emission line morphology as a function of SMBH mass (M_{BH}) and Eddington ratio (L/L_{Edd}), shown in Fig. 3. In the

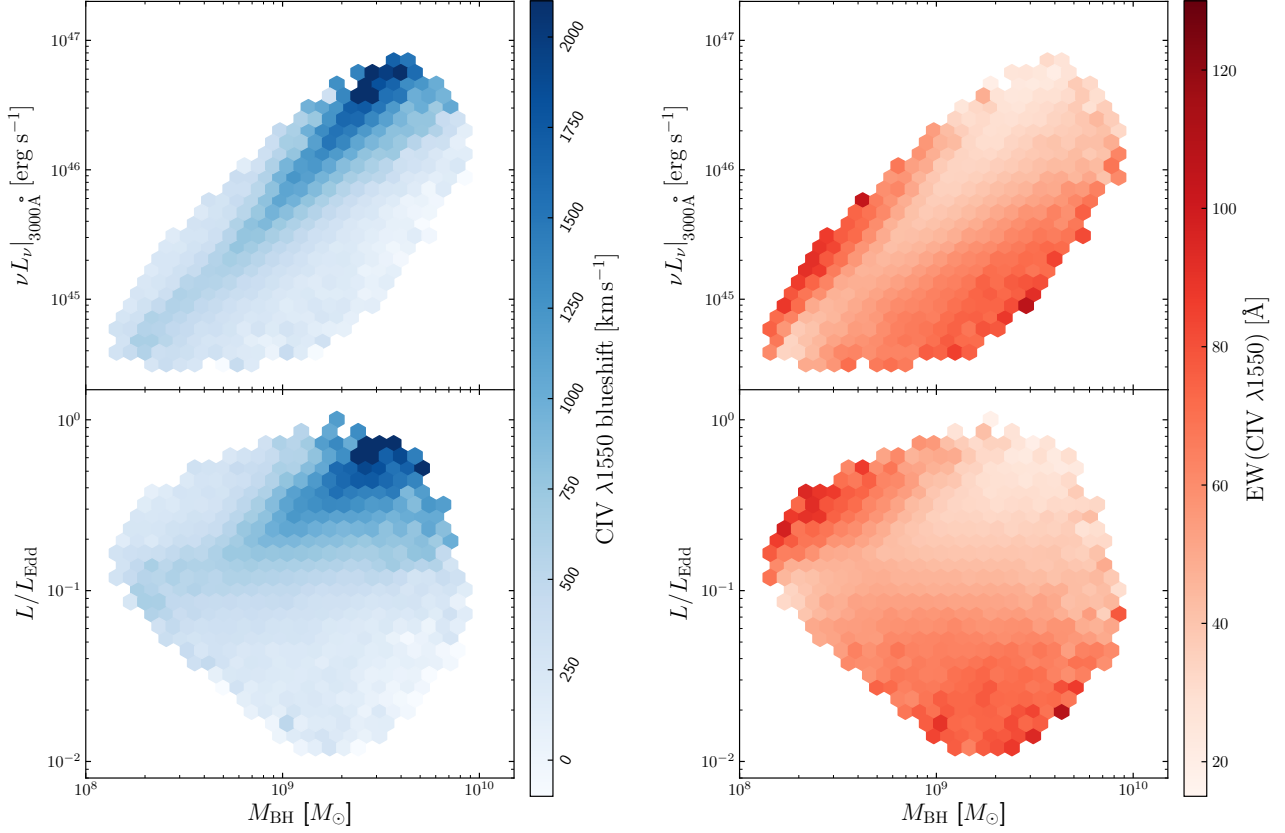


Figure 3. The median observed C IV blueshift (left) and EW (right) in bins of SMBH mass, 3000 Å ultraviolet continuum luminosity (top) and Eddington ratio (bottom). Data are shown only for bins which contain five or more objects. The C IV blueshift and EW are seen to anti-correlate: areas of parameter space with strong blueshifts have weak EW and vice versa. $L/L_{\text{Edd}} \geq 0.1$ is a necessary but not sufficient condition for observing the largest C IV blueshifts. The strongest C IV blueshifts are observed only at large SMBH mass and large Eddington ratio, while high EW C IV emission is observed at large Eddington ratio and smaller mass. The Baldwin effect can be observed in the sense that objects with brighter 3000 Å luminosities tend to have weaker C IV EWs on average. However, the C IV EW behaviour as a function of M_{BH} and L/L_{Edd} shows that the underlying drivers of the Baldwin effect are more complicated than a simple dependence on the ultraviolet luminosity.

left panel, we show the C IV emission line blueshift (as defined in Eq. 1) and in the right panel the EW of C IV. In the top panels, consistent with previous works, we find that more luminous quasars show weaker emission line strengths relative to the continuum and stronger emission line blueshifts. However, when considering the observed C IV properties as a function of both M_{BH} and L/L_{Edd} (bottom panel), we see a more complicated behaviour. To observe the strongest C IV blueshifts (which are associated with the smallest EWs), we need to look at objects with both $M_{\text{BH}} \gtrsim 10^9 M_{\odot}$ and $L/L_{\text{Edd}} \gtrsim 0.1$. Moreover, the contours of constant C IV blueshift follow acute-angled ‘wedge’ shapes, which are somewhat orthogonal to lines of constant luminosity (running diagonally top-left to bottom-right in the $M_{\text{BH}}-L/L_{\text{Edd}}$ space). At the same time, objects with the strongest C IV EWs $\gtrsim 100 \text{ \AA}$, which have strong symmetric emission with little or no blueshift, are found at high $L/L_{\text{Edd}} \gtrsim 0.1$ and relatively low $M_{\text{BH}} \lesssim 10^9 M_{\odot}$, and also at low $L/L_{\text{Edd}} \lesssim 0.03$.

To help us to understand the physical drivers behind the trends seen in C IV, in Figs. 4 and 5 we also show α_{OX} and He II EW across the same $M_{\text{BH}}-L/L_{\text{Edd}}$ parameter space. The α_{OX} behaviour is as expected from previous works (e.g. Mitchell et al. 2022), largely with more luminous objects displaying relatively weaker X-ray emission which is quantified by a more negative α_{OX} . A more interesting result is seen in the EW of He II, which is even more striking than the

behaviour seen in C IV. With the He II EW, there is a clear transition around $L/L_{\text{Edd}} \approx 0.1$, with both the strongest and weakest line emission only seen above this threshold. Below this Eddington limit, there is little change in the average line properties as a function of mass, but at $L/L_{\text{Edd}} \gtrsim 0.1$ there is a strong mass dependence with diagonal wedge-shaped contours similar to those observed in C IV. By contrast, the contours of constant α_{OX} are much less closely aligned with contours of constant C IV blueshift.

To test the robustness of these trends, we divide the $M_{\text{BH}}-L/L_{\text{Edd}}$ into square bins of 0.1 by 0.1 dex and compute the median absolute deviation (MAD) in each bin. The typical MAD is 285 km s⁻¹ in C IV blueshift, 13 Å in C IV EW and 0.49 Å in He II EW. The typical scatter within each bin is therefore significantly less than the dynamic range in the average emission line properties shown in Figs. 3 and 5, meaning that one is unlikely to find individual objects which go against the overall trend of the population. Dividing through by the median in each bin, the typical MAD/median in each bin is 0.29 and 0.26 for the He II and C IV EWs respectively, meaning that the typical range of emission line EW within each $M_{\text{BH}}-L/L_{\text{Edd}}$ bin is a factor of 3.5 and 3.8 for He II and C IV respectively, compared with the dynamic range of more than a factor of six seen in the median per-bin line properties.

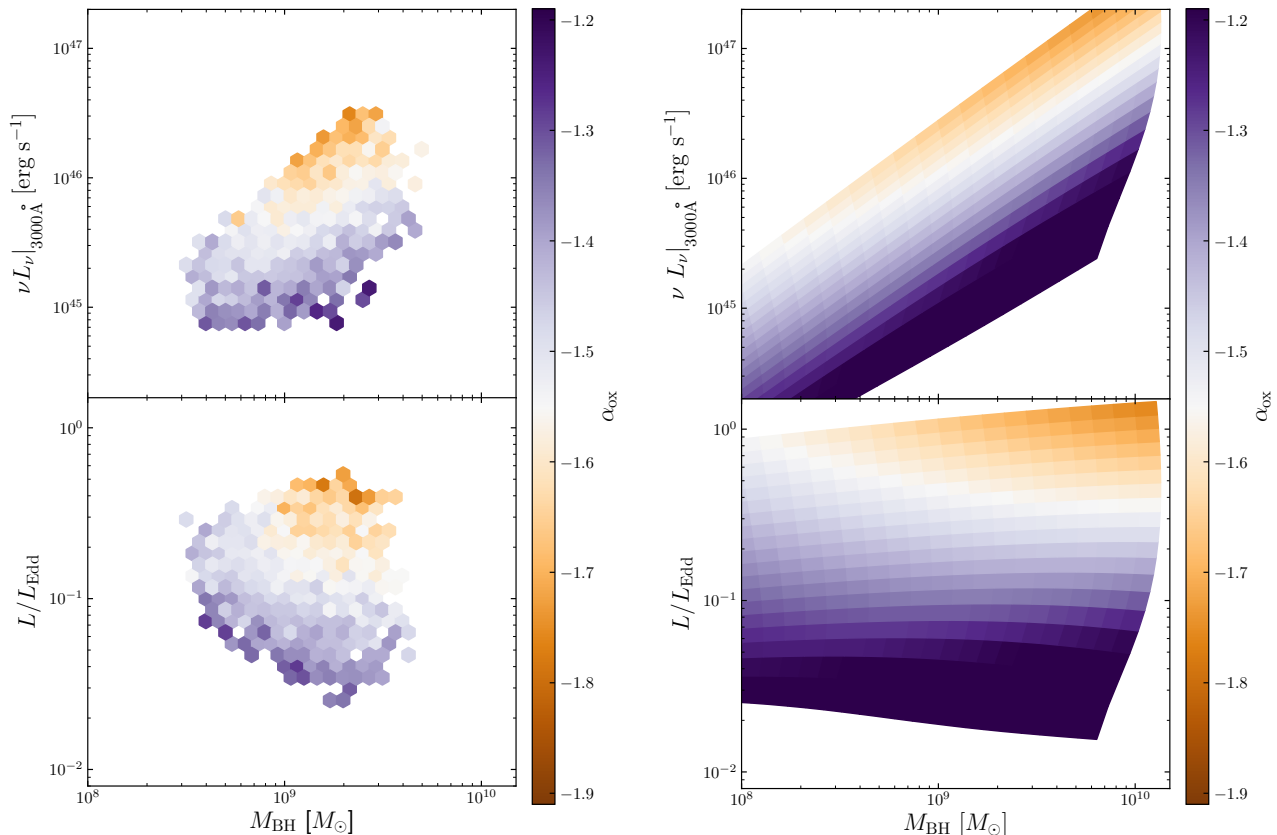


Figure 4. *Left panel:* The median observed α_{ox} in bins of SMBH mass, 3000 Å ultraviolet continuum luminosity (top) and Eddington ratio (bottom) for the 5031 objects from our sample with 2 keV X-ray measurements. Data are shown only for bins which contain five or more objects. *Right panel:* the predicted α_{ox} from low spin qSOSED models in the same parameter space. The observations show good agreement with the models, with α_{ox} more negative (i.e. more X-ray weak) in objects with brighter ultraviolet luminosities. In Fig. D1 we show equivalent models but with high spin, which do not show such agreement with the observations, suggesting that the $z \approx 2$ SDSS quasar population may be more consistent with low SMBH spins on average.

4.2 Comparison with model SEDs

In the right-hand panels of Figs. 4 and 5 we show how α_{ox} and L_{228}/L_{1640} , respectively, vary with mass and Eddington fraction, as modeled by qSOSED. These plots can be compared to the respective plots from the observational sample (left-hand panels), albeit with some caveats regarding bolometric corrections (Section 5.1.1) and M_{BH} estimates (Section 5.1.2). In a qualitative sense, the models do a reasonably good job of reproducing the trends observed in the data. Focusing first on α_{ox} , we can see that the general trend of decreasing α_{ox} with Eddington fraction is reproduced, and, in addition, the gradient is stronger at high M_{BH} , as observed in the data. To put this another way, in both the data and model results, the contour of fixed α_{ox} curves around, from being nearly horizontal at high M_{BH} to being closer to vertical at low M_{BH} . The dynamic range of model α_{ox} values is comparable to that observed, but the models do not produce soft enough spectra to match the data; $\alpha_{\text{ox}} \approx -1.9$ can be found in some bins in the quasar sample but the minimum value of α_{ox} in the models is -1.79 .

The comparison of the model L_{228}/L_{1640} ratio and the observed He II $\lambda 1640$ EW is also broadly encouraging, at least at relatively high Eddington fractions. This finding is perhaps more interesting as the He II EW is probing a portion of the SED that is not accessible directly. The basic behaviour, of decreasing He II EW with M_{BH} at high Eddington fractions, is well matched by the models. The models

also capture the diagonal contours of constant He II EW, in which the transition to low He II EWs occurs at higher masses for higher Eddington fractions. As discussed above, at low Eddington fractions ($L/L_{\text{Edd}} \lesssim 0.1$), something fundamentally switches in the data, with gradients generally being shallower and along a different direction in the parameter space. This relatively sharp change is not reproduced by the models, and may be telling us something fundamental about the quasar accretion process (see Section 5.2.1 for a discussion).

5 DISCUSSION

We have quantified the average behaviour of C IV $\lambda 1549$, He II $\lambda 1640$ and α_{ox} as a function of both M_{BH} and L/L_{Edd} , and compared our observations with predictions from qSOSED models. In this section we now discuss these results. We first outline the key caveats in our findings (Sections 5.1.1 and 5.1.2), before discussing possible interpretations of our results within the context of AGN accretion and outflow theories (Sections 5.2.1 and 5.2.2). Finally, we discuss some wider implications and possible future applications (Section 5.3), before summarizing our key conclusions in Section 6.

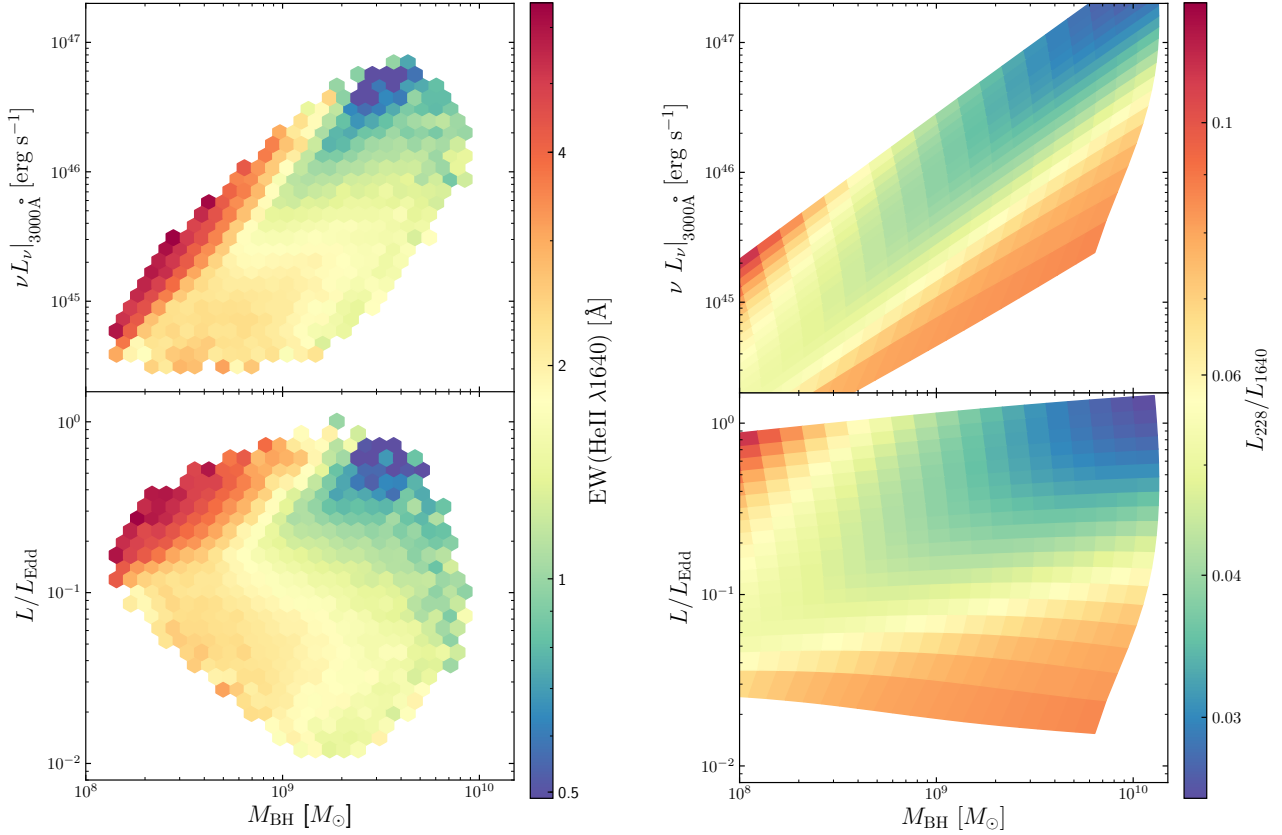


Figure 5. *Left panel:* The median observed He II EW in bins of SMBH mass, 3000 Å ultraviolet continuum luminosity (top) and Eddington ratio (bottom). Data are shown only for bins which contain five or more objects. *Right panel:* the predicted strength of He II ionizing photons at 228 Å relative to the 1640 Å continuum from QSOSED models. Above an Eddington ratio of ≈ 0.1 , there is a strong trend as a function of SMBH mass, with high mass objects showing the weakest He II emission and low mass objects showing the strongest He II emission. The model predictions show qualitatively similar behaviour in this region of parameter space, explaining the diagonal contours in constant He II. Below $L/L_{\text{Edd}} \lesssim 0.1$, the observed He II displays much weaker trends, and does not agree with the model predictions, suggesting that in this regime either the SED models are less accurate or the structure of the BLR is changing.

5.1 Key assumptions and limitations

5.1.1 Bolometric corrections

A large part of this work has attempted to quantify the ‘unseen’ extreme ultraviolet (EUV) portion of the SED which is not directly observable, but which can instead be probed via the He II emission line. This portion of the SED contributes a significant amount to the bolometric luminosity of a quasar. To estimate bolometric luminosities (and Eddington ratios $L_{\text{bol}}/L_{\text{Edd}}$), we have assumed a constant bolometric correction $f_{\text{bol}} \equiv L_{\text{bol}}/L_{3000}$ of 5.15, consistent with previous works in the literature (e.g. Richards et al. 2006; Krawczyk et al. 2013). However, we have also shown that the He II strength is changing as a function of M_{BH} and L/L_{Edd} , so we expect the strength of the EUV continuum and hence the bolometric correction to be varying with M_{BH} and L/L_{Edd} . Using our QSOSED models, we attempt to quantify this effect in Fig. 6. While our chosen value of $f_{\text{bol}} = 5.15$ lies within the range of values spanned by our grid of model SEDs, there is variation of around a factor of two in f_{bol} depending on the values of M_{BH} and L/L_{Edd} we consider. While this could in principle lead to systematic biases in our estimation of L/L_{Edd} , we show in Appendix C that these biases are likely to be small compared to the magnitude of the trends we observe.

We can however, briefly describe what might happen if we were to adopt a non-constant bolometric correction when inferring L/L_{Edd}

from our observations. For two objects, both at $\dot{m} = 0.2$, the f_{bol} inferred from the QSOSED models would be ≈ 6 and ≈ 3 for $M_{\text{BH}} = 10^8 M_{\odot}$ and $10^{10} M_{\odot}$ respectively. This would skew the observations in Fig. 5, moving the location of the strongest He II EW (at low M_{BH}) to larger L/L_{Edd} , more in line with the L/L_{Edd} threshold at high M_{BH} above which we see the weakest He II and largest C IV blueshifts.

5.1.2 Black hole mass estimates

As well as the assumption of a constant bolometric correction, we have used a single-epoch virial estimator to estimate SMBH masses throughout this work. The caveats associated with such estimates are numerous and have been reviewed by Shen (2013). Here we discuss some of the issues which are most relevant to our method and results. Most notably, the BLR radius–luminosity relation (as encoded through the virial f factor) may depend on the shape of the SED. Other uncertainties arising from (for example) orientation are likely to be random, in the sense that they will add scatter to our M_{BH} estimates but should not bias our results. While it is possible that our observed distribution of quasars in the $M_{\text{BH}}-L/L_{\text{Edd}}$ plane is not the same as the intrinsic distribution, the fact that we do still observe such striking behaviour in the He II and C IV emission line properties as a function of our inferred M_{BH} and L/L_{Edd} is telling

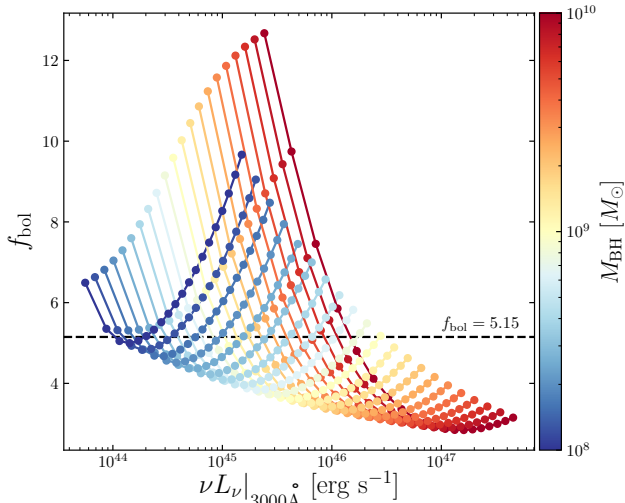


Figure 6. The predicted bolometric correction, $f_{\text{bol}} \equiv L_{\text{bol}}/L_{3000}$, as a function of L_{3000} , from QSOSED models. The points are colour-coded by M_{BH} with a logarithmic normalisation, and points of constant mass are joined with solid lines so that the trends with Eddington ratio can be understood by following individual lines from left to right. The adopted bolometric correction in this work, $f_{\text{bol}} = 5.15$, is shown as a horizontal dashed line. f_{bol} ranges from $\approx 3 - 10$, and our adopted f_{bol} is bounded by this range; however f_{bol} does have a clear dependence on mass and luminosity in the model SEDs. Our assumption of a fixed f_{bol} could lead to an artificially reduced dynamic range in the inferred L_{bol} at $M_{\text{BH}} = 10^8 M_{\odot}$ and an artificially increased range of L_{bol} at $M_{\text{BH}} = 10^{10} M_{\odot}$.

us that any random scatter or noise in our M_{BH} estimates is small enough not to ‘wash out’ the observed trends.

We used the FWHM of the Mg II line to estimate M_{BH} . Shen et al. (2008) showed that such Mg II-derived M_{BH} estimates correlate tightly with those derived from H β across the full $10^{8-10} M_{\odot}$ mass range, with the distribution of $\log(M_{\text{BH}}^{\text{H}\beta}/M_{\text{BH}}^{\text{Mg II}})$ following a Gaussian with mean 0.034 and dispersion 0.22 dex. Shen & Liu (2012) extended this analysis to higher redshifts and higher luminosities, more appropriate for the objects in this work, and again found that the Mg II properties remained well correlated with those of H β . The Mg II-derived M_{BH} estimates we use in this work are therefore unlikely to be biased compared to those which we would have derived from a single-epoch H β measurement. The possibility remains, however, that such estimates are biased as a function of the SED, or equivalently, as a function of M_{BH} and L/L_{Edd} .

Early concerns about the universality of the BLR radius–luminosity relation were discussed by Kaspi et al. (2005) and Collin et al. (2006). More recently, various authors have tried to account for possible SED-dependent biases in single-epoch M_{BH} estimates (Du & Wang 2019; Dalla Bontà et al. 2020; Fonseca Alvarez et al. 2020; Martínez-Aldama et al. 2020), either using the accretion rate directly or by using the strength of optical iron emission $R_{\text{Fe II}}$ as a proxy. However, Khadka et al. (2022a,b) and Yu et al. (2022a) find the opposite result, with the inclusion of $R_{\text{Fe II}}$ having no effect on the scatter in either the Mg II or H β radius–luminosity relations.

While the literature is divided, we argue it is still true that any SED-dependent bias in our single-epoch M_{BH} estimates must be contained within the scatter on the BLR radius–luminosity relation, i.e. within 0.3–0.5 dex. This scatter is smaller than the range spanned by our

sample by a factor of ≈ 3 , meaning that SED-dependent biases in our M_{BH} cannot explain the observed trends presented in Section 4.1.

5.2 Quasar physics

5.2.1 AGN accretion models

In Section 4.2, we compared our observations with predictions from the QSOSED models of Kubota & Done (2018). The predictions for α_{OX} made by these models have recently been tested over a much broader parameter space ($M_{\text{BH}} \approx 10^7-10^{10} M_{\odot}$ and $L_{3000} \approx 10^{43.5-47} \text{ erg s}^{-1}$) by Mitchell et al. (2022), who find that the QSOSED model predicts the optical and X-ray SED fairly well for $M_{\text{BH}} \lesssim 10^9 M_{\odot}$, but that at higher masses the outer accretion disc spectra are predicted to be too cool to match the observed data, especially at lower Eddington ratios. This finding is consistent with our result (in Fig. 4) that the 2 keV emission is predicted to be slightly stronger (relative to the 2500 Å emission) than observed at $M_{\text{BH}} \approx 10^{9.5} M_{\odot}$.

In this work we have also quantified the He II emission, which provides a new, complementary probe of the ionizing SED across the $M_{\text{BH}}-L/L_{\text{Edd}}$ space. In Section 4.2 we found that, for $L/L_{\text{Edd}} \gtrsim 0.1$, the observed He II EW is qualitatively similar to the behaviour of the 54 eV ionizing SED predicted by the QSOSED models. The observations are consistent with a scenario in which (at least for $L/L_{\text{Edd}} \gtrsim 0.1$) the strength of He II emission is set directly by the ionizing photon luminosity at 54 eV, and thus that He II is providing a probe of the EUV which is not directly observable. Moreover, the observed He II EW behaviour provides further evidence for the soft excess to be an intermediate, warm Comptonising component which behaves in the way in which the QSOSED models predict. The strongest and weakest 228 Å emission (relative to the 1640 Å continuum) are both produced at high Eddington ratios, at low ($\approx 10^8 M_{\odot}$) and high ($\approx 10^{10} M_{\odot}$) SMBH mass respectively.

However, the match between the observed He II and the predicted strength of the 54 eV ionizing luminosity is not perfect, especially at $L/L_{\text{Edd}} \lesssim 0.1$. Intriguingly, this L/L_{Edd} regime is similar to the region of the $M_{\text{BH}}-L_{2500 \text{ Å}}$ space where Mitchell et al. (2022) find a mismatch between the observed and predicted α_{OX} , which could suggest that the SED models are inaccurate in this part of the $M_{\text{BH}}-L/L_{\text{Edd}}$ parameter space. However, this regime is also where the He II and C IV EWs appear to be less well correlated, in the sense that the C IV EW increases towards the lowest Eddington ratios on our sample, while the He II EW is observed to have more moderate values at $L/L_{\text{Edd}} < 0.1$. The observations could therefore indicate a decoupling between the He II EW and the 228 Å continuum flux at these Eddington ratios, perhaps if changes in the BLR covering factor lead to differences in the fraction of the continuum source which is reprocessed into emission lines. Another possibility is that the He II continuum becomes optically thin, for instance if the density of the BLR were to decrease (which could indicate the absence of a dense outflow). Either way, the observed switch in He II behaviour above and below $L/L_{\text{Edd}} \approx 0.1$, which is not reflected in the QSOSED models, suggests that a fundamental change occurs in the structure of either the BLR or the accretion flow.

C IV is a resonant doublet with a more complicated ionic structure than He II. However, the close correspondence of the C IV blueshift with the He II EW, allied with the fact that the He II behaviour can be consistently explained with trends in the SED, suggests that the C IV morphology is governed by accretion physics - specifically the shape of the SED in the near and extreme ultraviolet regions. Given the proximity of the relevant C IV and He II ionization edges, at 48 and 54 eV respectively, this result is perhaps unsurprising.

5.2.2 AGN outflow models

In this subsection we test the predictions made by [Giustini & Proga \(2019\)](#), who summarize current understanding of AGN accretion and outflow mechanisms with a particular focus on the physical conditions required to drive powerful winds from the accretion disc through radiation line driving. We note again that the picture described by [Giustini & Proga \(2019\)](#) might not be the only plausible model for AGN outflows, but we choose to compare with their picture as it provides clear testable predictions within a well-defined framework. In particular, [Giustini & Proga \(2019\)](#) suggest that both $L/L_{\text{Edd}} \gtrsim 0.25$ and $M_{\text{BH}} \gtrsim 10^8 M_{\odot}$ are required to power strong outflows from AGN through radiation line driving: below these thresholds the X-ray flux is strong enough to over-ionize material and the ultraviolet flux will be too low to accelerate a line-driven wind.

For the purposes of this comparison, we assume that any blue-wing excess in the C IV emission line profile is tracing an outflow along the line-of-sight from the accretion disc, and hence that the blueshift presented in Fig. 3 is a measure of the strength of emission from the outflowing wind ([Leighly & Moore 2004](#); [Richards et al. 2011](#)). The origin of the C IV emission line blueshift is still debated (see [Gaskell & Goosmann 2013, 2016](#), for an alternative view), but a growing body of work is connecting the C IV emission morphology with more unambiguous tracers of line driven winds. For example, the strengths and velocities of broad C IV absorption troughs have been shown to correlate with the C IV emission blueshift ([Rankine et al. 2020](#); [Rodríguez Hidalgo & Rankine 2022](#)), and the velocities of narrow C IV line-locked ‘triplet’ absorption features are also strongly correlated with the emission blueshift ([Rankine et al. in preparation](#)).

For the discussion in this subsection, we therefore assume that objects with larger C IV blueshifts have stronger disc winds. To be more precise, the C IV blueshift is taken as a measure of the strength of emission from outflowing gas relative to the strength of emission from virialized gas at the systemic redshift. In this paradigm, the trends seen in Fig. 3 are in good agreement with the picture proposed by [Giustini & Proga \(2019\)](#). We see large ($\gtrsim 1000 \text{ km s}^{-1}$) median C IV blueshifts only in bins with high SMBH masses *and* high Eddington ratios. Furthermore, we do indeed see a more complicated mass dependence above $L/L_{\text{Edd}} \approx 0.2$. High L/L_{Edd} is therefore a necessary, but not sufficient, condition for observing large C IV blueshifts, consistent with the results of [Baskin & Laor \(2005\)](#).

In detail, we only observe strong outflow signatures in objects with $M_{\text{BH}} \gtrsim 10^9 M_{\odot}$, which is somewhat higher than the criterion of $M_{\text{BH}} \gtrsim 10^8 M_{\odot}$ proposed by [Giustini & Proga \(2019\)](#). Requiring $M_{\text{BH}} \gtrsim 10^9 M_{\odot}$ and $L/L_{\text{Edd}} \gtrsim 0.2$ together ensures that the criterion $L_{\text{bol}} \gtrsim 10^{45.5} \text{ erg s}^{-1}$ is satisfied. Above this L_{bol} threshold, [Zakamska & Greene \(2014\)](#) suggest that quasar winds are capable of driving ionized gas (as traced by [O III] $\lambda 5008$ emission) beyond the escape velocity of the host galaxy. The kinematics of C IV and [O III] are known to correlate ([Coatman et al. 2019](#)), and our observed C IV blueshift behaviour is therefore consistent with the conclusion of [Zakamska & Greene \(2014\)](#) that $L_{\text{bol}} \gtrsim 10^{45.5} \text{ erg s}^{-1}$ is required for quasar feedback to operate.

For $10^8 M_{\odot} \lesssim M_{\text{BH}} \lesssim 10^9 M_{\odot}$ and $L/L_{\text{Edd}} \gtrsim 0.1$, we see the strongest He II and strongest non-outflowing C IV line emission. One possible explanation for this behaviour would be that this emission represents ionized material which has been launched from the accretion disc, but lacks the ultraviolet luminosity to accelerate the outflow, meaning that such material falls back and virializes instead of escaping. In such a scenario the strong symmetric emission from high-ionization ultraviolet lines would represent a failed line-driven wind, analogous to models of the low-ionization BLR which repre-

sent a failed dust-driven wind ([Czerny & Hryniewicz 2011](#); [Baskin & Laor 2018](#), see also [Elvis 2017](#)).

While we observe a reasonably good qualitative agreement between the C IV blueshift behaviour and the [Giustini & Proga \(2019\)](#) predictions for line-driven winds, the reality is likely more complicated. In particular, [Giustini & Proga \(2019\)](#) do not consider any emission from a ‘soft excess’. Instead they assume that the ionizing SED consists of just two components, emitted from a thermal disc and a hot corona. Such a simple model is unlikely to explain our observational results: the different behaviour of He II EW and α_{ox} as a function of M_{BH} and L/L_{Edd} points to the presence of a third spectral component in the EUV which can vary separately from the disc and corona.

Other physical effects could also be at play. In particular, as the accretion rate increases above $\dot{m} \gtrsim 0.3$, we expect the disc structure to transition between geometries akin to slim discs and thin discs ([Abramowicz et al. 1988](#); [Abramowicz & Fragile 2013](#)). At low accretion rates, slim discs are well approximated by the [Novikov & Thorne \(1973\)](#) thin disc solution, as used in QSOSED, but we expect this to be less accurate as \dot{m} increases. In other words, the regime in which QSOSED appears to best match our data is also the regime in which we might expect it to be least accurate. The origin of the apparent transition around $L/L_{\text{Edd}} \approx 0.1$ in Figs. 3 and 5 is therefore still uncertain and further work is required to fully understand the interplay between AGN accretion flows, the ionizing SEDs they produce, and the outflows they drive.

Line-driven winds from high Eddington ratio AGN are often cited as a potentially important component of radiative-mode (quasar-mode) feedback ([Zubovas & King 2012](#)). While difficult to observe directly, such feedback modes are required to regulate galaxy growth and explain the tight SMBH-galaxy correlations observed in the local universe (see [Fabian 2012](#), for a review). However, most SMBHs in the local universe do not have masses above $10^9 M_{\odot}$, so our results might suggest that the line-driven winds traced by C IV cannot have a significant effect on their host galaxies’ growth and co-evolution as they never reach the SMBH masses required to launch strong winds. There are at least two solutions to this apparent problem. First is that radiative-mode feedback could still be operating through ionized gas outflows, but that the gas is in a different ionization phase and is not seen in C IV, but instead in other bands such as the X-ray ‘ultra-fast outflows’ ([Laha et al. 2021](#)). Second could be that quasar-mode feedback is only effective when coupled to dusty gas ([Fabian et al. 2008](#); [Ishibashi et al. 2018](#); [Ricci et al. 2022](#)), thus having most impact when the AGN is obscured by dust ([Temple et al. 2019](#); [Lansbury et al. 2020](#); [Jun et al. 2021](#); [Assef et al. 2022](#)).

5.2.3 SMBH spin and system inclination

In our QSOSED modeling, we kept inclination fixed at $\cos i = 0.5$ and only presented the non-spinning SMBH case, $a_* = 0$. However, both of these parameters have an impact on the predicted SEDs. The impact of SMBH spin is particularly pronounced; plots matching those in the right-hand panels of Figs. 4 and 5 are presented in Appendix D. The basic finding from the maximal spin models is that the observed trends of α_{ox} with mass and Eddington fraction are not reproduced, for reasons that are explained in Appendix D. In fact, all of the maximal spin models have $\alpha_{\text{ox}} \gtrsim -1.5$, meaning that the X-ray luminosity is always quite high compared to the optical and ultraviolet, and the observed soft spectra at high mass and high Eddington fraction are not reproduced for $a_* = 1$. If there are a significant proportion of maximally spinning SMBHs in our quasar sample, this would imply that the model predictions are not valid

for high spin objects, potentially undermining many of the results discussed in Section 5.2.1. Alternatively, if the QSOSED models are correct, the good agreement at low spin and poor agreement at high spin would imply that most SDSS quasars at $z \approx 2$ typically have low or moderate SMBH spins.

SMBH spin is most commonly estimated from broad iron line emission in the X-ray band (Reynolds 2019). Spin measurements tend to be rather high, with the majority of X-ray measurements in AGN consistent with maximally spinning SMBHs. This apparent preference might initially appear to be inconsistent with our results. However, there are a number of factors at work. First, discs around maximally spinning SMBHs have higher radiative efficiencies and are thus more luminous. As shown in figure 3 of Reynolds (2019), this might lead to high spins being over-represented in a sample. One could also imagine further selection effects if spins are easier to measure when they are close to maximal and the iron line is broader. Second, the majority of spin measurements are at lower masses ($M_{\text{BH}} \lesssim 10^8 M_{\odot}$) than in our sample, with only a handful of spin measurements in our considered mass regime. In fact, there is some tentative evidence for a decrease of SMBH spin with increasing mass (Sisk-Reynés et al. 2022), behaviour that is expected if accretion is coherent at low masses and more incoherent at higher masses, as predicted by both semi-analytic models and hydrodynamic simulations (King et al. 2008; Sesana et al. 2014; Zhang & Lu 2019; Bustamante & Springel 2019). If our results do indeed favour low or moderate SMBH spins in luminous quasars, then they are consistent with this proposed trend, especially since it is the high-mass quasars which cannot be matched by the maximally spinning QSOSED models. Any conclusions drawn here should be treated with caution, given (i) the difficulties in obtaining reliable and unbiased spin measurements, and (ii) the lack of knowledge about the impact of spin on the EUV and X-ray regions of the quasar SED.

We fixed inclination in the QSOSED models, adopting $\cos i = 0.5$. Following Copernican reasoning, we expect AGN to have a random, isotropic distribution of viewing angles, in which case the mean viewing angle of all AGN is $\cos i = 0.5$. Factoring in obscuration by a putative ‘torus’ beyond some maximum inclination, and foreshortening/limb darkening of the disc continuum might be expected to bias this mean viewing angle to lower (more face-on) inclinations (e.g. Krolik & Voit 1998; Matthews et al. 2017). If we were to adopt a different inclination in QSOSED, we can think about how the model predictions would change.

The hard X-ray source in QSOSED is isotropic, whereas the warm and thermal components have a disc-like geometry and thus produced an observed luminosity $\propto \cos i$, such that lower inclinations have higher luminosities. The impact of inclination on the outputs from QSOSED can thus be straightforwardly understood. Changing inclination from $i_1 \rightarrow i_2$ results in a fractional change in L_{3000} of $(\cos i_2 / \cos i_1)$. Since, for a given input \dot{m} , we calculate L/L_{Edd} from L_{3000} , we obtain a linear scaling of the y-axis of the right-hand panels of Figs 5 and 4 by the same factor. The change in α_{ox} is $\Delta\alpha_{\text{ox}} = -0.3838 \log_{10}(\cos i_2 / \cos i_1)$; adopting a lower inclination with $\cos i = 0.75$ would result in a more negative α_{ox} in all simulation bins by ≈ 0.07 . Finally, the ratio L_{228}/L_{1640} undergoes small changes with $\cos i$, but these are fairly uniform across the simulation grid and thus unimportant, given that the proportionality constant between L_{228}/L_{1640} and He II EW is not known. Furthermore, the He II EW depends on the L_{228} seen by the He II gas, rather than the L_{228} seen by a distant observer, meaning that the true inclination dependence of He II EW would depend on the BLR geometry. We have explicitly checked that the anticipated changes in L_{3000} and α_{ox}

are indeed reproduced in QSOSED, except for small departures in the α_{ox} due to contamination of the 2 keV flux by the warm component.

5.3 Wider implications and future work

5.3.1 Comparison with other populations

Recent work has attempted to compare the ultraviolet emission properties in high redshift ($z \gtrsim 6$) quasars with their lower redshift analogues (Mazzucchelli et al. 2017; Meyer et al. 2019; Shen et al. 2019; Schindler et al. 2020; Yang et al. 2021b; Lai et al. 2022; Wang et al. 2022). Such quasars are (by selection) very luminous, and generally display large C IV blueshifts. From our results, we would argue that comparative studies should match AGN samples not just in luminosity, but in two independent parameters which trace L/L_{Edd} and M_{BH} . Stepney et al. (in preparation) will discuss this further in a study of C IV and He II emission in SDSS quasars with redshifts $z > 3.5$.

Current samples of $z \gtrsim 6$ quasars include a significant number of objects with inferred $L/L_{\text{Edd}} > 1$, which lie outside the parameter space explored in this work. We have verified that the sample of 37 quasar spectra with redshifts $z > 6.3$ presented by Yang et al. (2021b) typically show narrower Mg II profiles than $z \approx 2$ SDSS objects with the same 3000 Å luminosities, suggesting smaller M_{BH} and larger L/L_{Edd} (for a given L_{3000}) than the quasars characterized in this work. For such objects it is therefore not surprising that their typical ultraviolet emission properties are different from the majority of the SDSS population at $z \approx 2$.

The X-ray properties of the $z > 6$ quasar population appear to be consistent with the $\alpha_{\text{ox}}-L_{2500\text{Å}}$ relation seen at lower redshifts (Nanni et al. 2017; Vito et al. 2019; Pons et al. 2020, 2021). To gain further insight, we encourage future works to consider the behaviour of α_{ox} as a function of both M_{BH} and L/L_{Edd} simultaneously.

5.3.2 BLR metallicities

The relative strengths of many ultraviolet emission lines are known to correlate with the C IV and He II emission properties (Richards et al. 2011; Temple et al. 2020). In particular, the flux ratios of high ionization ultraviolet lines such as C IV, N V $\lambda 1240$ and Si IV $\lambda 1400$ are tightly correlated with the C IV blueshift and He II EW (Temple et al. 2021b). Assuming no changes in density or ionization structure or geometry of the BLR, changes in these line ratios are sometimes taken to reflect changes in the metal content of the BLR (Nagao et al. 2006). Such an interpretation, combined with the results in this work, gives rise to a paradigm where the metal content of quasar BLRs is largest in objects with the largest M_{BH} and L/L_{Edd} , as noted by Xu et al. (2018) and Śniegowska et al. (2021) respectively.

However, as shown in Temple et al. (2021b), the variation in these line ratios can be explained with changes in the density of the emitting gas, and need not involve changes in metallicity (see also appendix A4 of Casebeer et al. 2006). In particular, the ultraviolet emission line ratios seen in objects with large C IV blueshifts can be explained by emission from relatively dense gas which is located closer to the ionizing source, while the line ratios in objects with high EW, symmetric C IV emission are consistent with emission from less dense gas at larger radii. Given the trends seen in Figs. 3 and 5, this is a much more natural explanation: objects with different SMBH masses and accretion rates have different accretion flows, which give rise to different EUV SEDs (as traced by He II) and different kinematic and density structures in the BLR (traced by the C IV blueshift and high ionization line ratios respectively). Under this alternative paradigm the BLR metallicity would be free to vary independently of M_{BH} and

L/L_{Edd} , and need not be super-solar in the early universe (cf. [Lai et al. 2022](#); [Wang et al. 2022](#)).

5.3.3 Quasar cosmology

Quasars are visible out to large cosmological distances, and display remarkably homogeneous behaviour across cosmic time. A growing body of work has proposed the non-linear scaling between the ultraviolet and X-ray continuum fluxes (i.e. the $\alpha_{\text{OX}}-L_{2500\text{\AA}}$ relation) as a way to use quasars as standardizable candles for cosmological measurements ([Risaliti & Lusso 2015, 2017, 2019](#); [Lusso & Risaliti 2017](#); [Salvestrini et al. 2019](#); [Lusso et al. 2020](#); [Sacchi et al. 2022](#); [Khadka & Ratra 2022](#)). However, [Petrosian et al. \(2022\)](#) have recently raised concerns about such methods. In this work we have shown that the ultraviolet emission lines provide further information which could be used to mitigate such concerns. With knowledge of the Mg II velocity width, and either the He II strength or the C IV properties, one should be able to locate an object in the $M_{\text{BH}}-L/L_{\text{Edd}}$ plane, and hence infer the intrinsic luminosity in a cosmology-independent way. By comparing to the observed fluxes one could then (in principle) infer a constraint on the Hubble parameter $H(z)$. However, further work is still required. In particular, we need to build a sample of quasars with ultraviolet emission line measurements which have independent measurements of the luminosity distance, in order to calibrate our $M_{\text{BH}}-L/L_{\text{Edd}}$ space in a cosmology-independent manner, in an analogous way to the use of the ‘inverse distance ladder’ to calibrate type Ia supernovae as standard candles (e.g. [Freedman et al. 2001](#); [Riess et al. 2021](#)).

5.3.4 Time variability and upcoming surveys

Changes in L/L_{Edd} for a quasar with fixed M_{BH} will lead to changes in the emitted spectrum, but such changes in SMBH fueling are expected to generally occur on the viscous time-scale, which is on the order of tens to thousands of years. However, SMBH accretion is inherently stochastic and the emitted flux varies by a factor of a few on shorter time-scales of just years. The time-scale and amplitude of this intrinsic ‘flickering’ are now known to depend on the SMBH mass and accretion rate ([Yu et al. 2022b](#)), and this stochastic flickering will contribute to the scatter within each binned region of our parameter space (Section 4.1).

In terms of spectroscopic variability, [Rivera et al. \(2020\)](#) showed that individual SDSS-RM quasars with multiple epochs of spectroscopy (i.e. with fixed M_{BH}) can vary in essentially every direction in the C IV blueshift–EW space, although objects with large blueshifts tend to show a change in blueshift and objects with strong EW show a change in EW. In the near future, SDSS-V ([Kollmeier et al. 2017](#)) will provide multi-epoch spectroscopic data for tens of thousands of luminous quasars, providing new insights into AGN variability.

At the same time, surveys such as DESI ([Alexander et al. 2023](#); [Chaussidon et al. 2023](#)) and 4MOST ([Merloni et al. 2019](#); [Eltvedt et al. 2023](#)) will probe fainter, yielding spectra of lower luminosity quasars than the sample investigated in this work, and future data releases from the *eROSITA* all-sky survey will include X-ray flux measurements for millions of AGN. Together these surveys will provide new constraints on the spectroscopic properties and ionizing SEDs of luminous AGN across the $M_{\text{BH}}-L/L_{\text{Edd}}$ parameter space.

6 CONCLUSIONS

We have investigated the rest-frame ultraviolet emission line properties in 186 303 SDSS quasars with redshifts $1.5 < z < 2.65$. We can infer α_{OX} , the logarithmic ratio of the rest-frame 2 keV and 2500 Å luminosities, for 5031 quasars in our sample. Using the FWHM of Mg II $\lambda 2800$ as a proxy for the virial velocity, we quantify the average properties of the C IV $\lambda 1549$ and He II $\lambda 1640$ emission lines across the two-dimensional space spanned by M_{BH} and L/L_{Edd} , and use these observations to confront qualitative predictions of when radiation-driven outflows should dominate kinetic feedback mechanisms ([Giustini & Proga 2019](#)) and theoretical SEDs arising from models of AGN accretion flows ([Kubota & Done 2018](#)). Our main conclusions are:

(i) As shown in previous works ([Richards et al. 2011](#); [Rankine et al. 2020](#)), the blueshift and EW of C IV correlate with the EW of He II. Objects with strong He II have high EW C IV with little or no blue excess, while objects with weaker He II show smaller EW C IV with larger C IV blueshifts.

(ii) We recover a Baldwin effect, but instead of simply correlating with the ultraviolet luminosity, we find that the C IV and He II properties display more complicated trends in the $M_{\text{BH}}-L/L_{\text{Edd}}$ plane. The dynamic range in He II EW is greatest at Eddington ratios ≥ 0.1 (Fig. 5). The largest C IV blueshifts are only observed at high L/L_{Edd} and high M_{BH} , while the highest EWs are seen only at high L/L_{Edd} and relatively low M_{BH} (Fig. 3). Composite spectra from these two extrema are shown in blue and green in Fig. 1.

(iii) In contrast to the ultraviolet emission line properties, but consistent with previous work in the literature, α_{OX} displays a simpler behaviour across the $M_{\text{BH}}-L/L_{\text{Edd}}$ plane (Fig. 4), albeit in a much smaller sample. α_{OX} shows a more direct correlation with the ultraviolet continuum luminosity than the emission lines, although α_{OX} does show some dependence on M_{BH} at fixed L_{3000} . Future data releases from *eROSITA*, SDSS-V and 4MOST will increase the number of known quasars with X-ray data.

(iv) Under the assumption that blueshifted C IV emission is tracing a disc wind accelerated by radiation line driving, we find our results are consistent with the global scheme for accretion and outflow mechanisms proposed by [Giustini & Proga \(2019\)](#). In particular, an Eddington-scaled mass accretion rate $\dot{m} \gtrsim 0.25$ is required for the formation of the strongest line-driven winds. [Giustini & Proga \(2019\)](#) suggest that $M_{\text{BH}} > 10^8 M_{\odot}$ is also required to launch strong line-driven winds, however we only observe the largest C IV blueshifts in objects with Mg II-inferred $M_{\text{BH}} \gtrsim 10^9 M_{\odot}$. Strong line emission at $M_{\text{BH}} \lesssim 10^9 M_{\odot}$ could perhaps indicate a ‘failed’ line-driven wind.

(v) Absent large changes in the density or geometry of the broad line region, the strength of He II is probing the strength of 54 eV ionizing radiation in the ‘unseen’ portion of the ultraviolet SED. Above $L/L_{\text{Edd}} \approx 0.1$, we find that the EW of He II is broadly consistent with the [Kubota & Done \(2018\)](#) Q_{SOSED} model. In other words, the relative strength of the 54 eV flux (which is photoionizing the broad line region) compared to the 1640 Å continuum is consistent with a relatively simple model where the strength of the ‘soft excess’ is adjusted to give the correct bolometric luminosity while keeping the strength of the hot coronal emission fixed at two per cent of the Eddington luminosity (as proposed by [Kubota & Done 2018](#)).

(vi) Below $L/L_{\text{Edd}} \approx 0.1$, something changes in the physics of the broad line region, with no strong C IV blueshifts observed and much weaker trends in He II. The Q_{SOSED} models do not provide as good a match to the observed He II EWs, consistent with the results of [Mitchell et al. \(2022\)](#) who find a discrepancy between the observed

and predicted α_{ox} in the same region of $M_{\text{BH}}-L/L_{\text{Edd}}$ parameter space.

(vii) Similar to Mitchell et al. (2022), we also find no strong evidence for high SMBH spins in our quasar sample: the zero-spin qSOSED models provide an acceptable match to the SED probes across a significant portion of our observed parameter space while the maximally spinning models do not. If a significant fraction of our quasar sample have maximally spinning SMBHs, this would suggest that the qSOSED model assumptions are not valid for high spin objects. Alternatively, taking the model results at face value would suggest low or moderate spins in typical SDSS quasars at $z \approx 2$.

ACKNOWLEDGEMENTS

We gratefully acknowledge useful discussions with Chris Done and Jake Mitchell. MJT thanks Chiara Mazzucchelli, Claudio Ricci and Roberto Assef for insightful comments, and Jinyi Yang for sharing the sample of $z > 6$ quasar spectra from Yang et al. (2021b). We thank Margherita Giustini, Ari Laor, Elisabeta Lusso and an anonymous referee for their useful feedback on the submitted manuscript.

MJT acknowledges support from a FONDECYT postdoctoral fellowship (3220516). JHM acknowledges funding from the Royal Society. ALR acknowledges support from UKRI (MR/T020989/1). This work made use of ASTROPY (Astropy Collaboration et al. 2013, 2018, 2022), MATPLOTLIB (Hunter 2007), and NUMPY (Harris et al. 2020).

Funding for the Sloan Digital Sky Survey IV has been provided by the Alfred P. Sloan Foundation, the U.S. Department of Energy Office of Science, and the Participating Institutions. SDSS-IV acknowledges support and resources from the Center for High-Performance Computing at the University of Utah. The SDSS web site is www.sdss.org.

SDSS-IV is managed by the Astrophysical Research Consortium for the Participating Institutions of the SDSS Collaboration including the Brazilian Participation Group, the Carnegie Institution for Science, Carnegie Mellon University, the Chilean Participation Group, the French Participation Group, Harvard-Smithsonian Center for Astrophysics, Instituto de Astrofísica de Canarias, The Johns Hopkins University, Kavli Institute for the Physics and Mathematics of the Universe (IPMU) / University of Tokyo, the Korean Participation Group, Lawrence Berkeley National Laboratory, Leibniz Institut für Astrophysik Potsdam (AIP), Max-Planck-Institut für Astronomie (MPIA Heidelberg), Max-Planck-Institut für Astrophysik (MPA Garching), Max-Planck-Institut für Extraterrestrische Physik (MPE), National Astronomical Observatories of China, New Mexico State University, New York University, University of Notre Dame, Observatório Nacional / MCTI, The Ohio State University, Pennsylvania State University, Shanghai Astronomical Observatory, United Kingdom Participation Group, Universidad Nacional Autónoma de México, University of Arizona, University of Colorado Boulder, University of Oxford, University of Portsmouth, University of Utah, University of Virginia, University of Washington, University of Wisconsin, Vanderbilt University, and Yale University.

For the purpose of open access, the authors will apply a Creative Commons Attribution (CC BY) licence to any Author Accepted Manuscript version arising from this submission.

DATA AVAILABILITY

The spectroscopic data underlying this article are available from SDSS.³ The X-ray data sets underlying this article are available from the references given in Section 2.2. The composite spectra in Fig. 1 are available as online supplementary material.

REFERENCES

- Abdurro'uf et al., 2022, *ApJS*, **259**, 35
 Abramowicz M. A., Fragile P. C., 2013, *Living Reviews in Relativity*, **16**, 1
 Abramowicz M. A., Czerny B., Lasota J. P., Szuszkiewicz E., 1988, *ApJ*, **332**, 646
 Alexander D. M., et al., 2023, *AJ*, **165**, 124
 Arnaud K. A., 1996, in Jacoby G. H., Barnes J., eds, *Astronomical Society of the Pacific Conference Series Vol. 101, Astronomical Data Analysis Software and Systems V*. p. 17
 Assef R. J., et al., 2022, *ApJ*, **934**, 101
 Astropy Collaboration et al., 2013, *A&A*, **558**, A33
 Astropy Collaboration et al., 2018, *AJ*, **156**, 123
 Astropy Collaboration et al., 2022, *ApJ*, **935**, 167
 Avni Y., Tananbaum H., 1982, *ApJ*, **262**, L17
 Avni Y., Tananbaum H., 1986, *ApJ*, **305**, 83
 Bachev R., Marziani P., Sulentic J. W., Zamanov R., Calvani M., Dultzin-Hacyan D., 2004, *ApJ*, **617**, 171
 Baldwin J. A., 1977, *ApJ*, **214**, 679
 Baldwin J. A., Netzer H., 1978, *ApJ*, **226**, 1
 Baskin A., Laor A., 2004, *MNRAS*, **350**, L31
 Baskin A., Laor A., 2005, *MNRAS*, **356**, 1029
 Baskin A., Laor A., 2018, *MNRAS*, **474**, 1970
 Baskin A., Laor A., Hamann F., 2013, *MNRAS*, **432**, 1525
 Begelman M. C., McKee C. F., Shields G. A., 1983, *ApJ*, **271**, 70
 Blandford R. D., Payne D. G., 1982, *MNRAS*, **199**, 883
 Boller T., Freyberg M. J., Trümper J., Haberl F., Voges W., Nandra K., 2016, *A&A*, **588**, A103
 Boroson T. A., Green R. F., 1992, *ApJS*, **80**, 109
 Bottorff M. C., Korista K. T., Shlosman I., 2000, *ApJ*, **537**, 134
 Brodzeller A., Dawson K., 2022, *AJ*, **163**, 110
 Bustamante S., Springel V., 2019, *MNRAS*, **490**, 4133
 Calistro Rivera G., et al., 2021, *A&A*, **649**, A102
 Casebeer D. A., Leighly K. M., Baron E., 2006, *ApJ*, **637**, 157
 Castor J. I., Abbott D. C., Klein R. I., 1975, *ApJ*, **195**, 157
 Chajet L. S., Hall P. B., 2013, *MNRAS*, **429**, 3214
 Chaussidon E., et al., 2023, *ApJ*, **944**, 107
 Coatman L., Hewett P. C., Banerji M., Richards G. T., 2016, *MNRAS*, **461**, 647
 Coatman L., Hewett P. C., Banerji M., Richards G. T., Hennawi J. F., Prochaska J. X., 2017, *MNRAS*, **465**, 2120
 Coatman L., Hewett P. C., Banerji M., Richards G. T., Hennawi J. F., Prochaska J. X., 2019, *MNRAS*, **486**, 5335
 Coffey D., et al., 2019, *A&A*, **625**, A123
 Collin S., Kawaguchi T., Peterson B. M., Vestergaard M., 2006, *A&A*, **456**, 75
 Comparat J., et al., 2020, *A&A*, **636**, A97
 Croom S. M., et al., 2002, *MNRAS*, **337**, 275
 Czerny B., Elvis M., 1987, *ApJ*, **321**, 305
 Czerny B., Hryniewicz K., 2011, *A&A*, **525**, L8
 Dalla Bontà E., et al., 2020, *ApJ*, **903**, 112
 Davidson K., Netzer H., 1979, *Reviews of Modern Physics*, **51**, 715
 Dibai E. A., 1980, *Soviet Ast.*, **24**, 389
 Done C., Davis S. W., Jin C., Blaes O., Ward M., 2012, *MNRAS*, **420**, 1848
 Du P., Wang J.-M., 2019, *ApJ*, **886**, 42
 Dwelly T., et al., 2017, *MNRAS*, **469**, 1065
 Eltvéd A. M., et al., 2023, *MNRAS*, **521**, 3384

³ <https://www.sdss4.org/dr17/>

- Elvis M., 2000, *ApJ*, **545**, 63
- Elvis M., 2017, *ApJ*, **847**, 56
- Elvis M., et al., 1994, *ApJS*, **95**, 1
- Emmering R. T., Blandford R. D., Shlosman I., 1992, *ApJ*, **385**, 460
- Fabian A. C., 2012, *ARA&A*, **50**, 455
- Fabian A. C., Vasudevan R. V., Gandhi P., 2008, *MNRAS*, **385**, L43
- Fawcett V. A., Alexander D. M., Rosario D. J., Klindt L., Lusso E., Morabito L. K., Calistro Rivera G., 2022, *MNRAS*, **513**, 1254
- Ferland G. J., et al., 2013, *Rev. Mex. Astron. Astrofis.*, **49**, 137
- Ferland G. J., et al., 2017, *Rev. Mex. Astron. Astrofis.*, **53**, 385
- Ferland G. J., Done C., Jin C., Landt H., Ward M. J., 2020, *MNRAS*, **494**, 5917
- Fonseca Alvarez G., et al., 2020, *ApJ*, **899**, 73
- Freedman W. L., et al., 2001, *ApJ*, **553**, 47
- Fu S., Brandt W. N., Zou F., Laor A., Garmire G. P., Ni Q., Timlin John D. I., Xue Y., 2022, *ApJ*, **934**, 97
- Fukumura K., Kazanas D., Contopoulos I., Behar E., 2010, *ApJ*, **715**, 636
- Gaskell C. M., 1982, *ApJ*, **263**, 79
- Gaskell C. M., Goosmann R. W., 2013, *ApJ*, **769**, 30
- Gaskell C. M., Goosmann R. W., 2016, *Ap&SS*, **361**, 67
- Giustini M., Proga D., 2019, *A&A*, **630**, A94
- Gordon C., Arnaud K., 2021, PyXspec: Python interface to XSPEC spectral-fitting program, Astrophysics Source Code Library, record ascl:2101.014 (ascl:2101.014)
- Haardt F., Maraschi L., 1991, *ApJ*, **380**, L51
- Harris C. R., et al., 2020, *Nature*, **585**, 357
- Hewett P. C., Wild V., 2010, *MNRAS*, **405**, 2302
- Higginbottom N., Proga D., Knigge C., Long K. S., Matthews J. H., Sim S. A., 2014, *ApJ*, **789**, 19
- Hoare M. G., Drew J. E., 1991, *MNRAS*, **249**, 452
- Hunter J. D., 2007, *Computing In Science & Engineering*, **9**, 90
- Ishibashi W., Fabian A. C., Ricci C., Celotti A., 2018, *MNRAS*, **479**, 3335
- Jensen T. W., et al., 2016, *ApJ*, **833**, 199
- Jin C., Ward M., Done C., Gelbord J., 2012, *MNRAS*, **420**, 1825
- Jun H. D., Assef R. J., Carroll C. M., Hickox R. C., Kim Y., Lee J., Ricci C., Stern D., 2021, *ApJ*, **906**, 21
- Just D. W., Brandt W. N., Shemmer O., Steffen A. T., Schneider D. P., Chartas G., Garmire G. P., 2007, *ApJ*, **665**, 1004
- Kaspi S., Maoz D., Netzer H., Peterson B. M., Vestergaard M., Jannuzi B. T., 2005, *ApJ*, **629**, 61
- Khadka N., Ratra B., 2022, *MNRAS*, **510**, 2753
- Khadka N., Martínez-Aldama M. L., Zajaček M., Czerny B., Ratra B., 2022a, *MNRAS*, **513**, 1985
- Khadka N., Zajaček M., Panda S., Martínez-Aldama M. L., Ratra B., 2022b, *MNRAS*, **515**, 3729
- King A. R., Pringle J. E., Hofmann J. A., 2008, *MNRAS*, **385**, 1621
- Kollmeier J. A., et al., 2017, arXiv e-prints, p. arXiv:1711.03234
- Konigl A., Kartje J. F., 1994, *ApJ*, **434**, 446
- Krawczyk C. M., Richards G. T., Mehta S. S., Vogeley M. S., Gallagher S. C., Leighly K. M., Ross N. P., Schneider D. P., 2013, *ApJS*, **206**, 4
- Krolik J. H., Kallman T. R., 1988, *ApJ*, **324**, 714
- Krolik J. H., Voit G. M., 1998, *ApJ*, **497**, L5
- Kruczek N. E., et al., 2011, *AJ*, **142**, 130
- Kubota A., Done C., 2018, *MNRAS*, **480**, 1247
- Kwan J., Krolik J. H., 1981, *ApJ*, **250**, 478
- Laha S., Reynolds C. S., Reeves J., Kriss G., Guainazzi M., Smith R., Veilleux S., Proga D., 2021, *Nature Astronomy*, **5**, 13
- Lai S., et al., 2022, *MNRAS*, **513**, 1801
- Lansbury G. B., Banerji M., Fabian A. C., Temple M. J., 2020, *MNRAS*, **495**, 2652
- Laor A., Davis S. W., 2014, *MNRAS*, **438**, 3024
- Leighly K. M., 2004, *ApJ*, **611**, 125
- Leighly K. M., Moore J. R., 2004, *ApJ*, **611**, 107
- Leighly K. M., Halpern J. P., Jenkins E. B., Casebeer D., 2007, *ApJS*, **173**, 1
- Liu T., et al., 2020, *ApJS*, **250**, 32
- Liu T., et al., 2022, *A&A*, **661**, A5
- Lusso E., Risaliti G., 2016, *ApJ*, **819**, 154
- Lusso E., Risaliti G., 2017, *A&A*, **602**, A79
- Lusso E., et al., 2020, *A&A*, **642**, A150
- Lusso E., et al., 2021, *A&A*, **653**, A158
- Lyke B. W., et al., 2020, *ApJS*, **250**, 8
- Lynden-Bell D., 1969, *Nature*, **223**, 690
- Maddox N., et al., 2017, *MNRAS*, **470**, 2314
- Marlar A., Shemmer O., Brotherton M. S., Richards G. T., Dix C., 2022, *ApJ*, **931**, 41
- Martínez-Aldama M. L., Zajaček M., Czerny B., Panda S., 2020, *ApJ*, **903**, 86
- Mathews W. G., Ferland G. J., 1987, *ApJ*, **323**, 456
- Matthews J. H., Knigge C., Long K. S., 2017, *MNRAS*, **467**, 2571
- Mazzucchelli C., et al., 2017, *ApJ*, **849**, 91
- Mejía-Restrepo J. E., Trakhtenbrot B., Lira P., Netzer H., 2018, *MNRAS*, **478**, 1929
- Merloni A., et al., 2019, *The Messenger*, **175**, 42
- Meyer R. A., Bosman S. E. I., Ellis R. S., 2019, *MNRAS*, **487**, 3305
- Mitchell J. A. J., Done C., Ward M. J., Kynoch D., Hagen S., Lusso E., Landt H., 2022, arXiv e-prints, p. arXiv:2210.11977
- Mizumoto M., Done C., Tomaru R., Edwards I., 2019, *MNRAS*, **489**, 1152
- Murray N., Chiang J., 1995, *ApJ*, **454**, L105
- Murray N., Chiang J., Grossman S. A., Voit G. M., 1995, *ApJ*, **451**, 498
- Nagao T., Marconi A., Maiolino R., 2006, *A&A*, **447**, 157
- Nanni R., Vignali C., Gilli R., Moretti A., Brandt W. N., 2017, *A&A*, **603**, A128
- Ni Q., et al., 2018, *MNRAS*, **480**, 5184
- Ni Q., et al., 2022, *MNRAS*, **511**, 5251
- Nomura M., Ohsuga K., 2017, *MNRAS*, **465**, 2873
- Nomura M., Ohsuga K., Done C., 2020, *MNRAS*, **494**, 3616
- Novikov I. D., Thorne K. S., 1973, in *Black Holes (Les Astres Occlus)*. pp 343–450
- Osterbrock D. E., Ferland G. J., 2006, *Astrophysics of gaseous nebulae and active galactic nuclei*
- Petrosian V., Singal J., Mutchnick S., 2022, *ApJ*, **935**, L19
- Petrucchi P. O., Ursini F., De Rosa A., Bianchi S., Cappi M., Matt G., Dadina M., Malzac J., 2018, *A&A*, **611**, A59
- Petrucchi P. O., et al., 2020, *A&A*, **634**, A85
- Pons E., McMahon R. G., Banerji M., Reed S. L., 2020, *MNRAS*, **491**, 3884
- Pons E., McMahon R. G., Banerji M., Reed S. L., 2021, *MNRAS*, **501**, 6208
- Proga D., 2007, *ApJ*, **661**, 693
- Proga D., Kallman T. R., 2004, *ApJ*, **616**, 688
- Proga D., Stone J. M., Kallman T. R., 2000, *ApJ*, **543**, 686
- Rankine A. L., Hewett P. C., Banerji M., Richards G. T., 2020, *MNRAS*, **492**, 4553
- Rankine A. L., Matthews J. H., Hewett P. C., Banerji M., Morabito L. K., Richards G. T., 2021, *MNRAS*, **502**, 4154
- Reynolds C. S., 2019, *Nature Astronomy*, **3**, 41
- Ricci C., et al., 2022, *ApJ*, **938**, 67
- Richards G. T., Vanden Berk D. E., Reichard T. A., Hall P. B., Schneider D. P., SubbaRao M., Thakar A. R., York D. G., 2002, *AJ*, **124**, 1
- Richards G. T., et al., 2006, *ApJS*, **166**, 470
- Richards G. T., et al., 2011, *AJ*, **141**, 167
- Riess A. G., Casertano S., Yuan W., Bowers J. B., Macri L., Zinn J. C., Scolnic D., 2021, *ApJ*, **908**, L6
- Risaliti G., Elvis M., 2010, *A&A*, **516**, A89
- Risaliti G., Lusso E., 2015, *ApJ*, **815**, 33
- Risaliti G., Lusso E., 2017, *Astronomische Nachrichten*, **338**, 329
- Risaliti G., Lusso E., 2019, *Nature Astronomy*, **3**, 272
- Rivera A. B., Richards G. T., Hewett P. C., Rankine A. L., 2020, *ApJ*, **899**, 96
- Rivera A. B., Richards G. T., Gallagher S. C., McCaffrey T. V., Rankine A. L., Hewett P. C., Shemmer O., 2022, *ApJ*, **931**, 154
- Rodríguez Hidalgo P., Rankine A. L., 2022, *ApJ*, **939**, L24
- Sacchi A., et al., 2022, *A&A*, **663**, L7
- Salvato M., et al., 2022, *A&A*, **661**, A3
- Salvestrini F., Risaliti G., Bisogni S., Lusso E., Vignali C., 2019, *A&A*, **631**, A120
- Schindler J.-T., et al., 2020, *ApJ*, **905**, 51
- Schneider D. P., et al., 2010, *AJ*, **139**, 2360

Scott J. E., Kriss G. A., Brotherton M., Green R. F., Hutchings J., Shull J. M., Zheng W., 2004, *ApJ*, **615**, 135

Sesana A., Barausse E., Dotti M., Rossi E. M., 2014, *ApJ*, **794**, 104

Shang Z., Wills B. J., Robinson E. L., Wills D., Laor A., Xie B., Yuan J., 2003, *ApJ*, **586**, 52

Shang Z., et al., 2005, *ApJ*, **619**, 41

Shen Y., 2013, *Bulletin of the Astronomical Society of India*, **41**, 61

Shen Y., Ho L. C., 2014, *Nature*, **513**, 210

Shen Y., Liu X., 2012, *ApJ*, **753**, 125

Shen Y., Greene J. E., Strauss M. A., Richards G. T., Schneider D. P., 2008, *ApJ*, **680**, 169

Shen Y., et al., 2011, *ApJS*, **194**, 45

Shen Y., et al., 2019, *ApJ*, **873**, 35

Sisk-Reynés J., Reynolds C. S., Matthews J. H., Smith R. N., 2022, *MNRAS*, **514**, 2568

Slone O., Netzer H., 2012, *MNRAS*, **426**, 656

Śniegowska M., Marziani P., Czerny B., Panda S., Martínez-Aldama M. L., del Olmo A., D’Onofrio M., 2021, *ApJ*, **910**, 115

Steffen A. T., Strateva I., Brandt W. N., Alexander D. M., Koekemoer A. M., Lehmer B. D., Schneider D. P., Vignali C., 2006, *AJ*, **131**, 2826

Stevens M. L., Shull J. M., Danforth C. W., Tilton E. M., 2014, *ApJ*, **794**, 75

Sulentic J., Marziani P., 2015, *Front. Astron. Space Sci.*, **2**, 6

Sulentic J. W., Zwitter T., Marziani P., Dultzin-Hacyan D., 2000, *ApJ*, **536**, L5

Sulentic J. W., Bachev R., Marziani P., Negrete C. A., Dultzin D., 2007, *ApJ*, **666**, 757

Sun J., Shen Y., 2015, *ApJ*, **804**, L15

Telfer R. C., Kriss G. A., Zheng W., Davidsen A. F., Tytler D., 2002, *ApJ*, **579**, 500

Temple M. J., Banerji M., Hewett P. C., Coatman L., Maddox N., Peroux C., 2019, *MNRAS*, **487**, 2594

Temple M. J., Ferland G. J., Rankine A. L., Hewett P. C., Badnell N. R., Ballance C. P., Del Zanna G., Dufresne R. P., 2020, *MNRAS*, **496**, 2565

Temple M. J., Banerji M., Hewett P. C., Rankine A. L., Richards G. T., 2021a, *MNRAS*, **501**, 3061

Temple M. J., Ferland G. J., Rankine A. L., Chatzikos M., Hewett P. C., 2021b, *MNRAS*, **505**, 3247

Temple M. J., Hewett P. C., Banerji M., 2021c, *MNRAS*, **508**, 737

Timlin J. D., Brandt W. N., Ni Q., Luo B., Pu X., Schneider D. P., Vivek M., Yi W., 2020, *MNRAS*, **492**, 719

Timlin John D. I., Brandt W. N., Laor A., 2021, *MNRAS*, **504**, 5556

Titarchuk L., 1994, *ApJ*, **434**, 570

Vanden Berk D. E., Wesolowski S. C., Yeckley M. J., Marciniak J. M., Quashnock J. M., Machia L. M., Wu J., 2020, *MNRAS*, **493**, 2745

Vasudevan R. V., Fabian A. C., 2007, *MNRAS*, **381**, 1235

Vasudevan R. V., Fabian A. C., 2009, *MNRAS*, **392**, 1124

Verner D. A., Ferland G. J., Korista K. T., Yakovlev D. G., 1996, *ApJ*, **465**, 487

Vestergaard M., Osmer P. S., 2009, *ApJ*, **699**, 800

Vestergaard M., Wilkes B. J., 2001, *ApJS*, **134**, 1

Vietri G., et al., 2018, *A&A*, **617**, A81

Vietri G., et al., 2020, *A&A*, **644**, A175

Vito F., et al., 2019, *A&A*, **630**, A118

Wang S., et al., 2022, *ApJ*, **925**, 121

Wild V., Hewett P. C., 2005, *MNRAS*, **358**, 1083

Wilkes B. J., 1984, *MNRAS*, **207**, 73

Wills B. J., Laor A., Brotherton M. S., Wills D., Wilkes B. J., Ferland G. J., Shang Z., 1999, *ApJ*, **515**, L53

Wolf J., et al., 2020, *MNRAS*, **492**, 3580

Wolfire M. G., Vallini L., Chevance M., 2022, *ARA&A*, **60**, 247

Woods D. T., Klein R. I., Castor J. I., McKee C. F., Bell J. B., 1996, *ApJ*, **461**, 767

Xu F., Bian F., Shen Y., Zuo W., Fan X., Zhu Z., 2018, *MNRAS*, **480**, 345

Yang X.-H., Ablimit K., Li Q.-X., 2021a, *ApJ*, **914**, 31

Yang J., et al., 2021b, *ApJ*, **923**, 262

York D. G., et al., 2000, *AJ*, **120**, 1579

Yu Z., et al., 2022a, arXiv e-prints, p. arXiv:2208.05491

Yu W., Richards G. T., Vogeley M. S., Moreno J., Graham M. J., 2022b, *ApJ*, **936**, 132

Zakamska N. L., Greene J. E., 2014, *MNRAS*, **442**, 784

Zanstra H., 1929, *Publs Dom. Ap. Obs. Victoria*, **4**, 209

Zappacosta L., et al., 2020, *A&A*, **635**, L5

Zhang X., Lu Y., 2019, *ApJ*, **873**, 101

Zhu Y., Bu D.-F., Yang X.-H., Yuan F., Lin W.-B., 2022, *MNRAS*, **513**, 1141

Zubovas K., King A., 2012, *ApJ*, **745**, L34

APPENDIX A: X-RAYS AND BLR PHOTOIONIZATION

This Appendix shows that the X-ray portion of the SED is an insignificant source of ionization for typical AGN emission line regions. This is surprising since the SEDs shown in Fig. 2 have a significant fraction of their power at high energies, and the ultraviolet–X-ray hardness ratio α_{OX} is known to correlate with emission line properties. However, photoionization is photon-counting, and there are relatively few X-ray photons despite their significant energy.

To illustrate this point, we use the hardest and softest SEDs from our model grid (Section 3), corresponding to $\dot{m} = 0.027$ and $\dot{m} = 1.000$ at $M_{\text{BH}} = 10^{10} M_{\odot}$. These SEDs are shown in the top panel of Figure A1, and have $\alpha_{\text{OX}} = -0.05$ and $\alpha_{\text{OX}} = -2.05$ respectively.

The photoionization rate for a given shell n is

$$\Gamma_n = \int_{\nu_0}^{\infty} \sigma_{\nu} \phi_{\nu} d\nu [\text{s}^{-1}] \quad (\text{A1})$$

where ν_0 , σ_{ν} , and ϕ_{ν} are the photoionization threshold of shell n , its energy-dependent photoionization cross section [cm^2], and the flux of ionizing photons [$\text{cm}^{-2} \text{s}^{-1} \text{Hz}^{-1}$] (Osterbrock & Ferland 2006). The total photoionization rate is the sum over all shells,

$$\Gamma_{\text{total}} = \sum_n \Gamma_n [\text{s}^{-1}] \quad (\text{A2})$$

The flux of ionizing photons ϕ_{ν} enters in the photoionization rate (Eq. A1). This is the ratio $\phi_{\nu} = 4\pi\nu J_{\nu}/(h\nu^2)$ and is shown in the lower panel of Fig. A1. The photon flux near 2 keV is typically ~ 6 dex fainter than the value near the peak.

The photon flux is multiplied by the photoionization cross section to derive the photoionization rate (Eq. A1). We concentrate on C^{2+} since photoionization of that ion produces C^{3+} and $\text{C IV } \lambda 1549$ emission. The shell-dependent cross sections for photoionization of C^{2+} , taken from Verner et al. (1996), are shown in Fig. A2. Both the $1s^2$ K shell in the X-ray and the lower energy $2s^2$ L shell are shown. Both shells have two electrons and, as expected, the peak photoionization cross sections are similar.

The photoionization rates for H^0 and the two shells of C^{2+} are listed in Table A1. The C^{2+} K-shell rate is 17 to 60 times smaller than the L-shell rate. Both are ~ 10 –30 times smaller than the H^0 photoionization rate. From this comparison we expect the ultraviolet continuum to play a more important role than the X-rays in the photoionization of the BLR, mainly due to the larger number of softer photons.

Figure A3 shows the rate at which photons interact with matter for our two reference SEDs and a solar composition. Calculations are done with Cloudy version 22.01, as last described by Ferland et al. (2017). Cloud parameters are typical of the C IV emitting region of an AGN, with a hydrogen density of 10^{10} cm^{-3} and an ionization parameter of $\log U = -2$. The vertical axis is the total light-matter interaction rate at a particular frequency and is the product of the photon flux and the total gas absorption opacity, evaluated for the appropriate chemical composition and degree of ionization. The 50–912 Å ultraviolet region is ~ 7 dex more interactive than 2 keV X-rays.

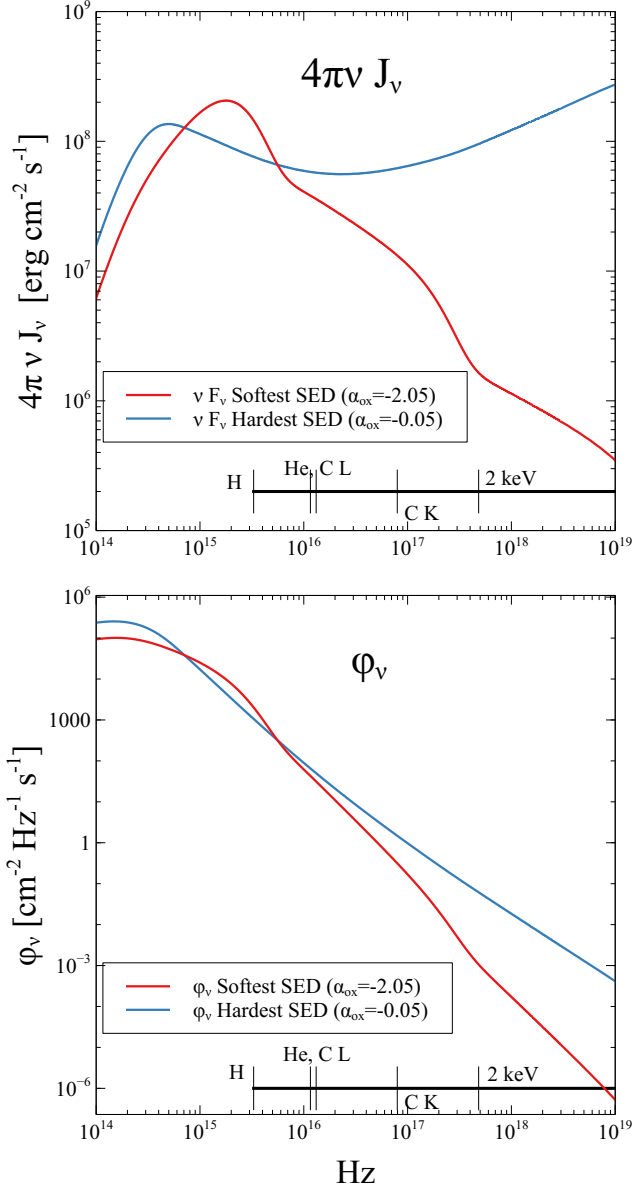


Figure A1. The upper panel shows the hardest and softest SEDs presented in this paper. The lower panel shows the flux of photons ϕ_ν for the same models. Some important energies are indicated by the hashed lines near the bottom of each panel. These show the ionization potentials of ground-state H^0 and He^{2+} , the L and K shells of C^{2+} , and 2 keV. The flux of ionizing photons is orders of magnitude smaller at 2 keV compared to the flux at the He II and C IV photoionization edges even for the hardest SED.

As stated above, photoionization is photon counting, and the relative paucity of X-ray photons cannot make up for their greater energy.

High-energy photons would dominate the physics if softer parts of the SED were extinguished so only X-rays strike the gas. Indeed, this is the ‘X-ray-dominated region’ (XDR) model of atomic and molecular regions of clouds exposed to ionizing radiation (Wolfire et al. 2022). It would be difficult to detect this XDR emission since emission from the gas which absorbed the softer radiation would be far stronger. This is discussed in Section 4.1 of Ferland et al. (2013). The ultraviolet luminosity of a realistic SED has more power than the relatively hard X-ray portion that drives an XDR. The full SED

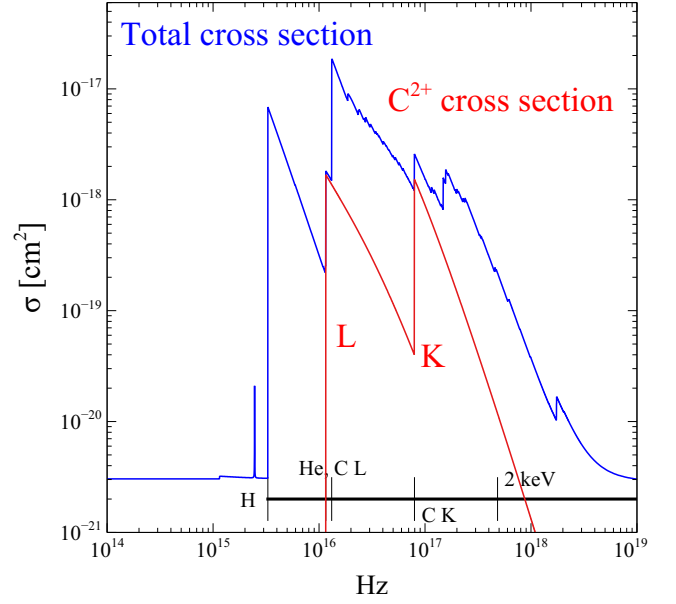


Figure A2. The K and L shell photoionization cross sections for C^{2+} are shown as a function of energy as the red line. The cross sections are from the calculations by Verner et al. (1996). The blue line shows the total (absorption and scattering) gas opacity rescaled to match the C^{2+} cross sections. The absorption opacity and the flux of photons (lower panel of Figure A1), determine the photoionization rate (Equation A1) and the effects of light upon matter shown in Figure A3.

Table A1. Photoionization rates for H^0 and the K and L shells of C^{2+} the hardest and softest SEDs. This allows us to compare the K-shell photoionization rate, produced by X-rays, with the L-shell rates, the result of the ultraviolet part of the SED. The photoionization rates are given for both the hardest and softest SED considered here. For both SEDs, the L-shell rates are more than 1 dex larger than K-shell rates, showing that the X-ray portion of the SED has comparatively little effect on the photoionization of C^{2+} .

Shell	$\Gamma_{\text{Softest}} [s^{-1}]$	$\Gamma_{\text{Hardest}} [s^{-1}]$
H^0 K	8.24e+00	5.52e+00
C^{2+} L	2.66e-01	4.66e-01
C^{2+} K	4.49e-03	2.71e-02

striking a cloud produces successive $H^+/H^0/H_2$ layers, which are brighter than the deep X-ray heated regions. Emission from regions powered by lower-energy light would dominate over the XDR. The penetrating X-rays, and galactic background cosmic rays, are important for producing the small electron fraction that is present in deep regions of a molecular cloud.

APPENDIX B: ADDITIONAL OBSERVATIONS

In this Appendix we present additional observational results. First, in Fig. B1 we present the He II EW, the C IV blueshift and α_{ox} as a function of the FWHM of Mg II λ 2800 and the 3000 Å continuum luminosity. These two parameters are measured directly from the SDSS spectroscopy and photometry respectively. By contrast, the

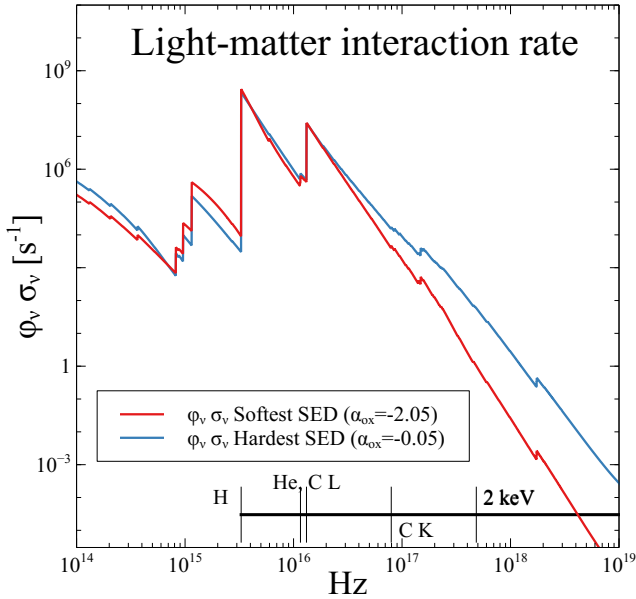


Figure A3. This shows the rate that photons interact with matter, the product of the flux of photons and the total gas opacity. X-rays interact with matter with a rate about ~ 7 dex slower than the rate near the peak rate around $50 - 912 \text{ \AA}$.

plots in the main text show observed properties as a function of

$$M_{\text{BH}} \propto L_{3000}^{0.5} \text{FWHM}_{\text{Mg II}}^2 \quad (\text{B1})$$

and

$$L/L_{\text{Edd}} \propto L_{3000}/M_{\text{BH}} \propto L_{3000}^{0.5} \text{FWHM}_{\text{Mg II}}^{-2} \quad (\text{B2})$$

Given that both M_{BH} and L/L_{Edd} depend on the observed parameters $\text{FWHM}_{\text{Mg II}}$ and L_{3000} , this might lead to induced correlations in the $M_{\text{BH}}-L/L_{\text{Edd}}$ space. However, in practice our inferred $M_{\text{BH}}-L/L_{\text{Edd}}$ space is simply a rotation and reflection of the $\text{FWHM}_{\text{Mg II}}-L_{3000}$ space, where we still see clear trends. Furthermore, we see the same He II behaviour in the X-ray detected sub-sample as in our full sample, meaning that our X-ray detected objects are not obviously biased compared to our full sample.

Second, we show the 2 keV X-ray continuum and He II $\lambda 1640$ line luminosities in Fig. B2. Assuming no changes in the BLR covering factor, and that the He II continuum is optically thick, $L_{\text{He II}}$ can be taken as a proxy for the continuum luminosity at 54 eV . These two observables show qualitatively different behaviour: contours of constant $L_{2 \text{ keV}}$ are largely aligned with lines of constant M_{BH} , which is consistent with the assumption in QSOSED that the hard X-ray power law component emits a constant fraction of the Eddington luminosity. He II behaves in a much more complex manner, with the gradient vector of increasing $L_{\text{He II}}$ changing depending on the location in the $M_{\text{BH}}-L/L_{\text{Edd}}$ space.

APPENDIX C: BOLOMETRIC CORRECTIONS

We have applied a fixed bolometric correction of 5.15 to estimate L_{bol} from $\nu L_\nu|_{3000 \text{ \AA}}$. In reality, the bolometric correction will vary as a function of M_{BH} and L/L_{Edd} . We discussed the variation of the bolometric correction from the QSOSED model grid in Section 5.1.1, showing a range in f_{bol} by a factor of $\approx 2-3$, where $f_{\text{bol}} \equiv \nu L_\nu|_{3000 \text{ \AA}}/L_{\text{bol}}$

is calculated from each individual QSOSED model. Although a true ‘Apples versus Apples’ comparison is only really possible with full knowledge of the intrinsic SED, in comparing our QSOSED models with data we tried to match scalings and biases in the data introduced by the fixed bolometric correction by applying appropriate transformations to the QSOSED outputs. Our single-epoch virial SMBH mass estimates make use of the observed Mg II line width, but also require an estimate of the line formation radius for which we follow the usual method and assume that the BLR radius scales as $R_{\text{BLR}} \propto L^{1/2}$. The L in this expression should really be some appropriate ionizing luminosity, but L_{bol} is normally used and we follow this convention. As a result, the bolometric correction enters into the SMBH mass estimate and implies a bias in the SMBH mass estimates with respect to the true SMBH mass by factor of $(f_{\text{bol}}/5.15)^{-1/2}$. As a result, when plotting M_{BH} along the x -axis of Figs. 5 and 4, we apply the scaling

$$M_{\text{BH}} = (f_{\text{bol}}/5.15)^{-1/2} M_{\text{BH}, \text{q}} \quad (\text{C1})$$

where $M_{\text{BH}, \text{q}}$ denotes the input QSOSED grid value (the ‘true’ SMBH mass). For L/L_{Edd} , correction factors appear in both the numerator and denominator. $L_{\text{Edd}} \propto M_{\text{BH}}$, introducing a bias factor $(f_{\text{bol}}/5.15)^{-1/2}$ into the Eddington ratio estimate, while the numerator is L_{bol} and so contains a straightforward bias factor of $f_{\text{bol}}/5.15$. As a result, the relationship between the L/L_{Edd} plotted in Figs. 5 and 4, and the dimensionless, Eddington-scaled accretion rate used as input to QSOSED is given by

$$L/L_{\text{Edd}} = \dot{m} \times (f_{\text{bol}}/5.15) \times (f_{\text{bol}}/5.15)^{-1/2} \quad (\text{C2})$$

The effect of introducing these scaling factors as transformations from the initial QSOSED grid is shown in Fig. C1, to show how the right-hand panels of Figs. 4 and 5 would change if we had made a different presentation choice. The scale factors twist and distort the simulation grid slightly from the original uniform parameter space, but, overall, the effects are fairly modest because only square-root terms distinguish the rightmost panel from the original input grid.

APPENDIX D: BLACK HOLE SPIN

In Fig. D1 we show how the predictions of α_{ox} and our He II $\lambda 1640$ EW proxy (L_{228}/L_{1640}) from QSOSED change if we instead consider a maximally spinning SMBH. While the qualitative trends in the L_{228}/L_{1640} are broadly in line with the low spin case, the $a_* = 1$ models fail to reproduce the observed low values of α_{ox} at high Eddington fractions and SMBH masses (see discussion in Section 5.2.3). The reason for this can be understood from the left-hand panel of Fig. D1, where we show the QSOSED broadband spectrum (the analogue to Fig. 2) for the maximally spinning case. Inspection of the high \dot{m} models in the top-panel reveals that the α_{ox} behaviour is driven by a combination of stronger X-rays and the movement of the peak of the thermal component. At high spin, the thermal peak moves blueward to higher energies, such that the lower frequency pivot point falls further from the peak and has lower flux compared to the low spin model. In QSOSED, this behaviour comes about in a slightly convoluted way, but is driven by the decrease of the radius R_{warm} (and corresponding temperature increase). This decrease happens because $R_{\text{warm}} = 2R_{\text{hot}}$, and R_{hot} must move inwards as spin increases, because R_{ISCO} moves closer to the SMBH so R_{hot} must also decrease from eq. 2 of Kubota & Done (2018) to maintain the model assumption that the dissipated power is 2 per cent of the Eddington luminosity. One could clearly construct other models in which the critical radii change in different ways when the spin is

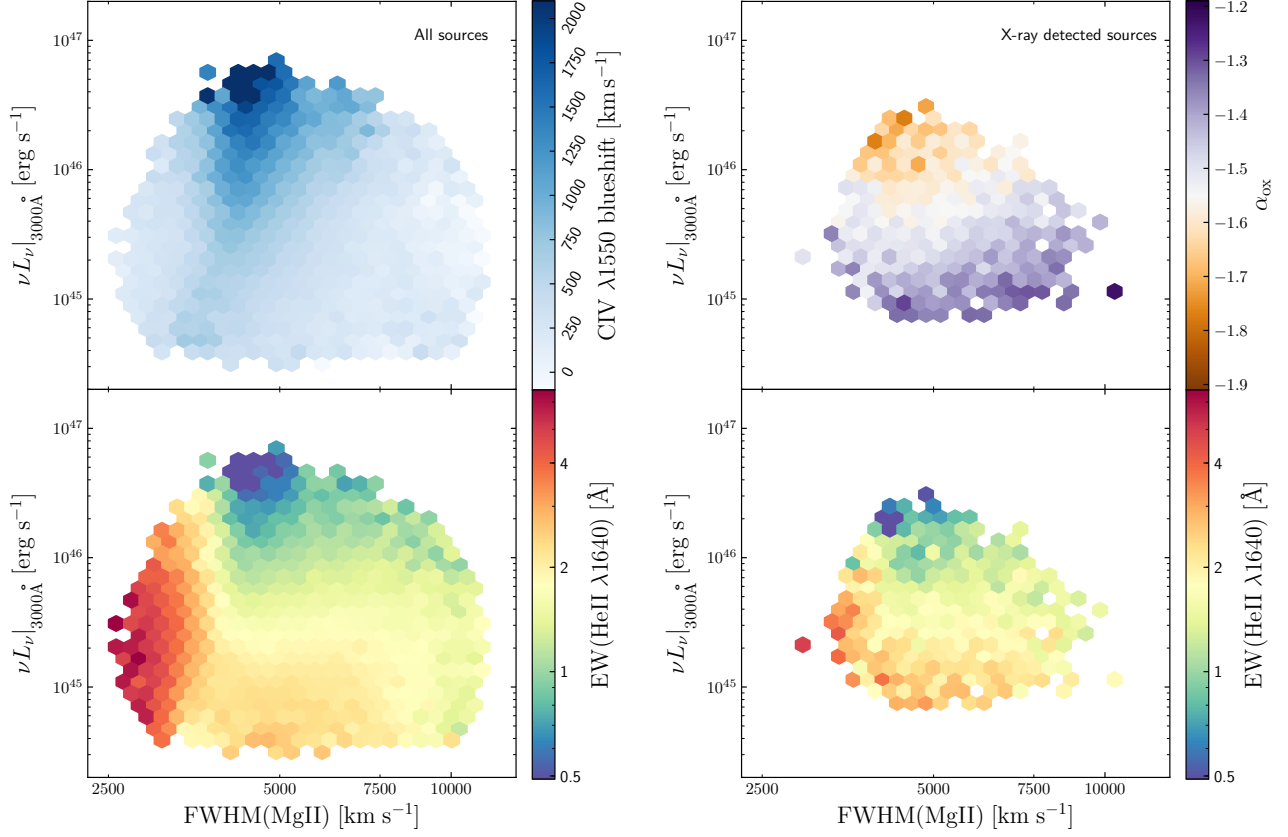


Figure B1. Observed quasar properties as a function of the FWHM of Mg II $\lambda 2800$ and the 3000 Å continuum luminosity. *Left panel:* The median He II EW (bottom) and C IV blueshift (top) in our full sample of 186 303 objects. *Right panel:* The median He II EW (bottom) and α_{ox} (top) in our sub-sample of 5031 X-ray detected sources. The He II behaviour is identical in both panels (modulo the sample size), suggesting that our X-ray detected sub-sample is not biased in terms of its ultraviolet emission properties. Moreover, clear differences are seen in the behaviour of He II and α_{ox} within the X-ray subsample: the strongest He II emission is seen only at low Mg II FWHM while the strongest 2 keV X-ray emission is seen only at the lowest 3000 Å luminosities.

changed, which is partly why we caution against over-interpreting the fact that maximal spins appear difficult to reconcile with the data.

This paper has been typeset from a $\text{\TeX}/\text{\LaTeX}$ file prepared by the author.

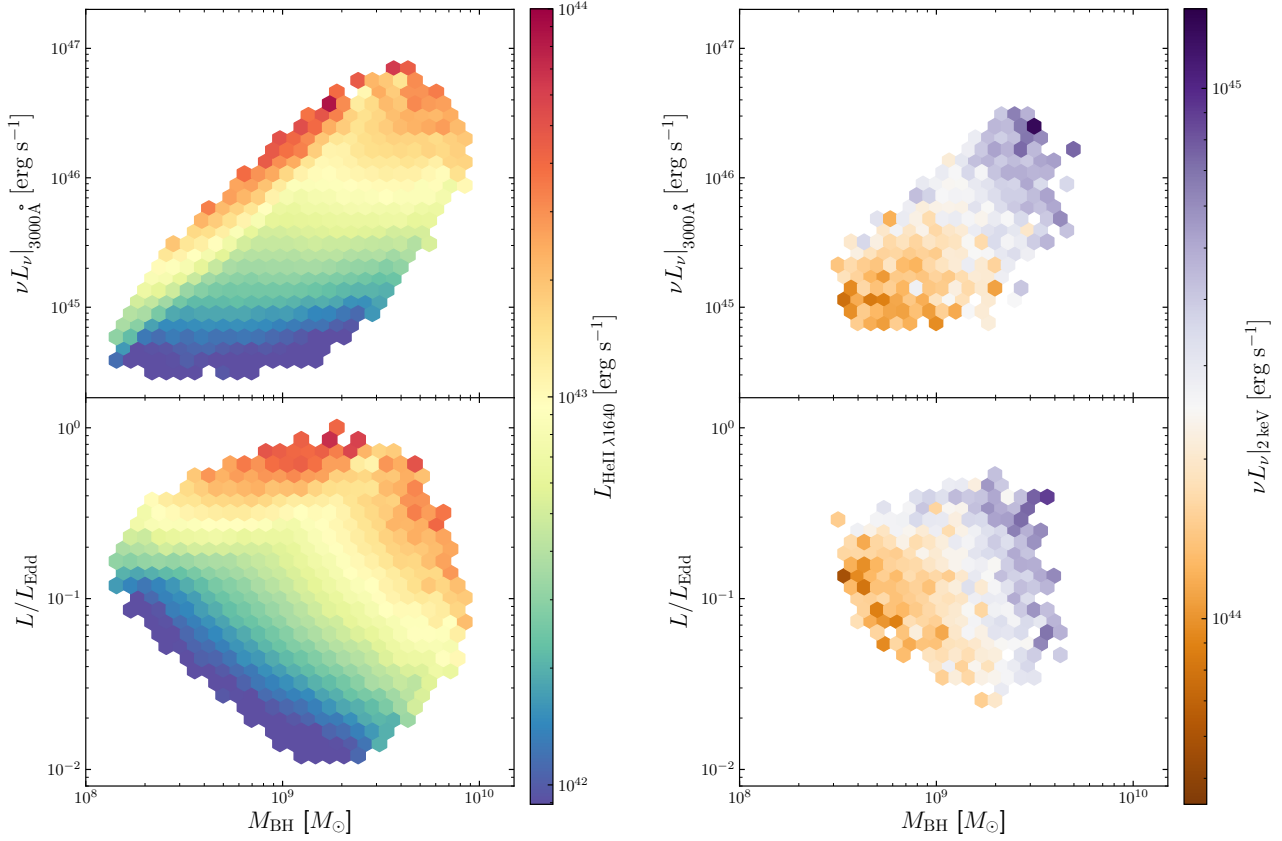


Figure B2. He II line luminosity (left) and 2 keV X-ray continuum luminosity (right) as a function of SMBH mass, luminosity and Eddington ratio. Contours of constant $L_{2 \text{ keV}}$ are largely aligned with lines of constant M_{BH} , consistent with the assumption in QSOSED that the hard X-ray emission is equal to 2 per cent of the Eddington limit.

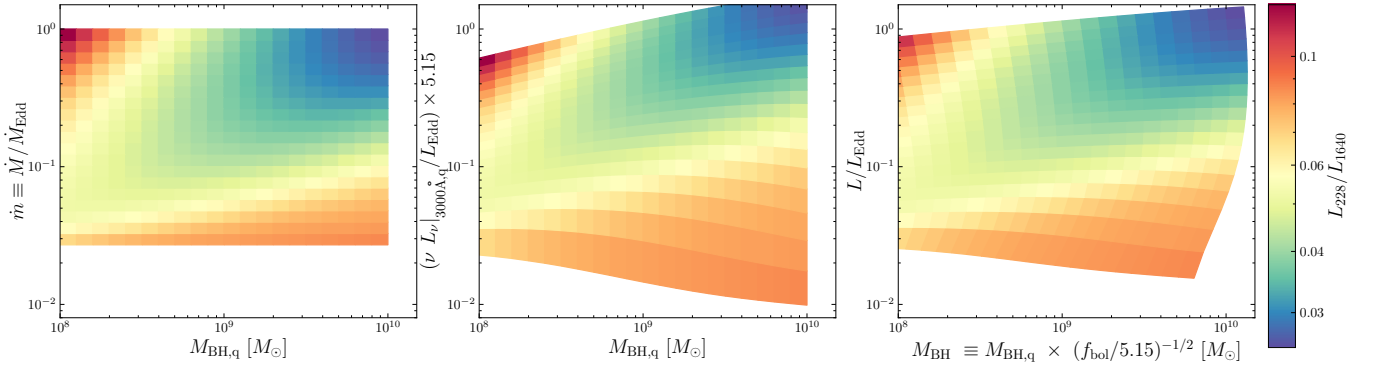


Figure C1. An illustration of how the QSOSED predictions change with differing treatments of the bolometric correction, focusing on the bottom-right panel of Fig. 4. *Left panel:* the model outputs plotted as a function of the intrinsic, input values of \dot{m} and $M_{\text{BH,q}}$. *Centre panel:* as in the left panel, but with the y-axis is replaced with $L_{\text{bol}}/L_{\text{Edd}}$ where L_{bol} is calculated from L_{3000} using a constant bolometric correction of 5.15. *Right panel:* as in the centre panel, but with the x-axis scaled by $(f_{\text{bol}}/5.15)^{-1/2}$ and the y-axis scaled by $(f_{\text{bol}}/5.15)^{1/2}$ to capture the impact of the bolometric correction on SMBH mass estimates in the observed data. See the main Appendix text for details.

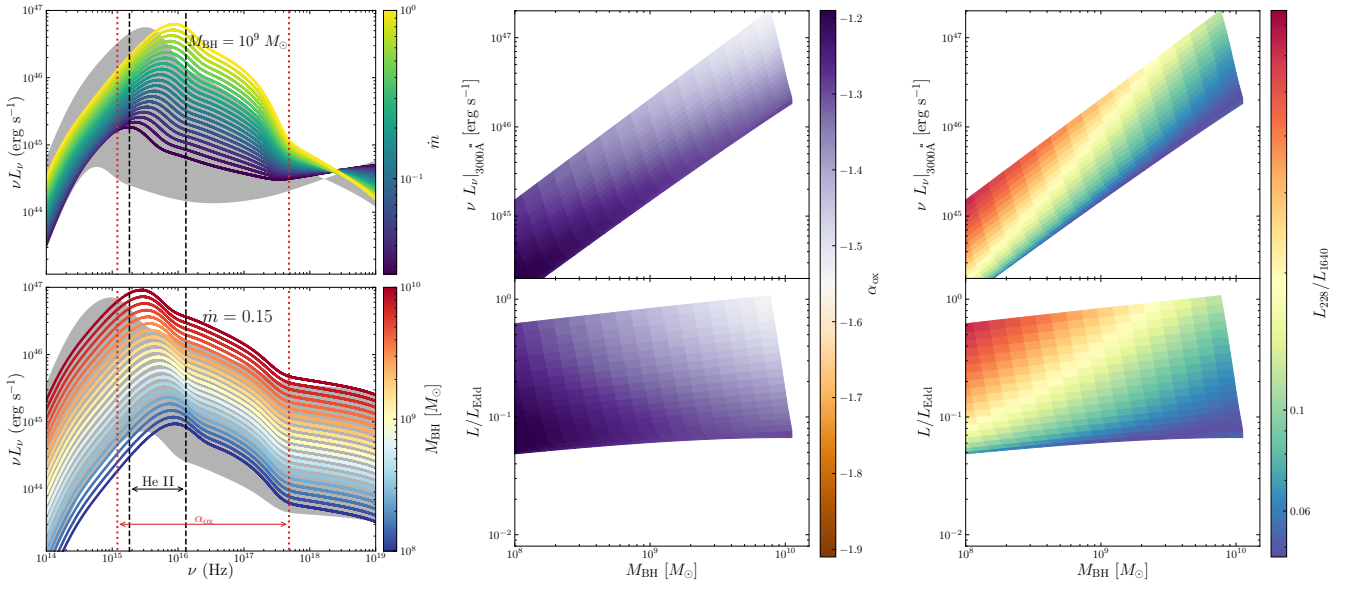


Figure D1. *Left panel:* As Fig. 2, but for the maximally spinning case, $a_* = 0.998$. The grey shaded area shows the range of the SEDs shown in Fig. 2 for the non-spinning case. *Centre and right panels:* QSOSED predictions for α_{ox} and L_{228}/L_{1640} for a maximally spinning SMBH with $a_* = 0.998$ (cf. Figs. 4 and 5).